Molecular basis and validation of the interactions of neuronal Mint proteins with Munc18-1 and their cellular interactome predicted by AlphaFold2

Saroja Weeratunga[1], Rachel S. Gormal[2], Meihan Liu[1], Denaye Eldershaw[1], Emma K. Livingstone[1], Anusha Malapaka[2], Tristan P. Wallis[2], Adekunle T. Bademosi[2], Anmin Jiang[2], Michael D. Healy[1], Frederic A. Meunier[2,3] and Brett M. Collins[1]*

[1]The University of Queensland, Institute for Molecular Bioscience, Queensland, 4072, Australia; [2]Clem Jones Centre for Ageing and Dementia Research, Queensland Brain Institute, The University of Queensland, Queensland, 4072, Australia; [3]The University of Queensland, School of Biomedical Sciences, Queensland, 4072, Australia;

Running Title: Interaction of Mints with Munc18-1

*Corresponding author:
Brett Collins, +61 (0)7 33462043, Email: b.collins@imb.uq.edu.au

Keywords – ARF3, AP3, neurexin, CASK, KCNJ, HXC9, USP22, calsyntenin, LRP, TJAP1, Munc18, Mint, X11, AlphaFold, SNARE, STXBP1, APP.

SUMMARY

Munc18-interacting proteins (Mints) are multi-domain adaptors that regulate neuronal membrane trafficking, signalling and neurotransmission. Mint1 and Mint2 are highly expressed in the brain and play overlapping roles in the regulation of synaptic vesicle fusion required for neurotransmitter release by interacting with the essential synaptic protein Munc18-1. The mechanism by which Mint1 mediates the interaction of Munc18-1 with Syntaxin1a (Sx1a) to control formation of the fusogenic SNARE complex and facilitate neurotransmission remains unclear. Here, we have studied both the specific interactions of the neuronal Mint proteins with Munc18-1 as well as their wider interactome. Using biochemical and biophysical binding approaches we identify a short acidic α-helical motif (AHM) within Mint1 and Mint2 that is necessary and sufficient for specific binding to Munc18-1. *In silico* modelling of this interaction with AlphaFold2 and extensive validation by structure-based mutagenesis showed that the AHM in Mint forms an α-helical structure that binds a conserved surface on Munc18-1 domain3b. In Munc18-1/2 double knockout cells we show that mutating the Mint-binding site significantly reduces the ability of Munc18-1 re-expression to rescue exocytosis. Although Munc18-1 can interact with Mint and Sx1a proteins simultaneously we find they have mutually reduced affinities, suggesting an allosteric coupling between the two proteins. Using AlphaFold2 we then examined the entire cellular network of putative interactions governed by the Mint scaffolds. Although this suggests many proposed binders do not associate directly with Mints, our analyses provide a structural model for their assembly with a variety of known and novel regulatory and cargo proteins including ARF3/ARF4 small GTPases, and the AP3 clathrin adaptor complex. Validation of Mint1 interaction with a new predicted binder TJAP1 provides experimental support that AlphaFold2 can correctly predict interactions across large-scale datasets. Overall, our data provides insights into the diversity of interactions mediated by the Mint family and shows that Mints may help facilitate a key trigger point in SNARE complex assembly and vesicle fusion.

INTRODUCTION

Synaptic vesicle fusion and release of neurotransmitters requires the formation of specific complexes between vesicular and plasma membrane SNARE proteins (soluble *N*-ethylmaleimide-sensitive factor attachment receptors). The vesicular v-SNAREs and target t-SNAREs form an α-helical coiled-coil assembly that provides the necessary energy to bring the two opposing lipid membranes together for membrane fusion. Munc18-1 (also called Munc18a, syntaxin-binding protein 1 (STXBP1), and neuronal Sec1 (nSec1)) is a member of the Sec1/Munc18 (SM) protein family, and an essential regulatory protein required for the assembly of this SNARE complex in neuronal membrane fusion. Munc18-1 binds with high affinity to the target or Qa-SNARE Syntaxin1a (Sx1a) and mediates both its trafficking and its incorporation into the SNARE complex with the Qbc-SNARE SNAP25 and the vesicle or R-SNARE Vamp2.

Importantly, Munc18-1 also interacts with other regulatory proteins including Munc13 and the two Munc-interacting protein (Mint) paralogues Mint1 and Mint2. Mints (also known as X11, amyloid precursor protein-binding family A (APBA) or Lin-10 proteins) are multi domain scaffolds that participate in a host of protein-protein interactions. The human genome encodes three Mint homologues, Mint1, Mint2 and Mint3 (Rogelj *et al*, 2006) (**Fig. 1A**). Mint1 and Mint2 are highly enriched in brain and spinal cord tissue, while Mint3 is ubiquitously expressed (Biederer *et al*, 2002; Ho *et al*, 2002b; Lee *et al*, 2003; Motodate *et al*, 2016; Tomita *et al*, 1999). Structurally, Mint proteins are composed of conserved C-terminal phosphotyrosine binding (PTB) and tandem PSD95/Dlg/ZO-1 (PDZ) domains and possess highly extended intrinsically disordered N-terminal domains that mediate paralogue-specific interactions. As scaffold proteins, the PTB domains of the Mint proteins interact with various ligands containing NPxY sequences (x is any amino acid) such as the amyloid precursor protein (APP), APP-like proteins APLP1 and APLP2, and TrkA (Borg *et al*, 1996; Borg *et al*, 1998; Caster & Kahn, 2013; Chaufty *et al*, 2012; Ho *et al*, 2008; Matos *et al*, 2012; Saito *et al*, 2011; Sakuma *et al*, 2009; Sullivan *et al*, 2014; Tomita *et al.*, 1999; Xie *et al*, 2013; Zhang *et al*, 2009; Zhang *et al*, 1997), while the PDZ domains of the Mint proteins bind to C-terminal PDZ binding motifs (PDZbms) in molecules including NMDA receptors, kalirin-7, neurexins, ApoER2 and LDLR (Biederer & Sudhof, 2000; Gotthardt *et al*, 2000; Jones *et al*, 2014; Minami *et al*, 2010; Motodate *et al*, 2019). The N-terminus of the Mint proteins contains both conserved and divergent sequences that mediate distinct protein-protein interactions. An N-terminal sequence specific to Mint1 called the CASK-interacting domain (CID) binds specifically to Ca^{2+}/calmodulin-dependent serine protein kinase (CASK/Lin-2) (a multi domain adapter and kinase) forming a tripartite complex with Veli/Lin-7 family proteins and neurexins at the pre-synapse (Borg *et al.*, 1998; Stafford *et al*, 2011; Tabuchi *et al*, 2002; Wu *et al*, 2020; Zhang *et al*, 2020). In contrast, the N-terminal regions of both neuronally expressed Mint1 and Mint2 proteins specifically interact with Munc18-1 via a sequence termed the Munc18-1-interacting domain (MID) (Biederer & Sudhof, 2000; Graham *et al*, 2011; Han *et al*, 2014; Ho *et al.*, 2002b; Okamoto & Sudhof, 1997, 1998; Park *et al*, 2012). However the mechanism of Munc18-1 interaction is unknown.

The importance of Mint proteins in neuronal function is apparent in studies showing homozygous deletions of Mint1 or Mint2 display disrupted GABAergic transmission (Ho *et al*, 2003; Sano *et al*, 2006), while knockout of both Mint1 and Mint2 neuronal isoforms leads to lethality at birth in most animals, with surviving mice displaying deficits in motor behaviours and spontaneous neurotransmitter release. A prominent phenotype of knockout animals is an alteration in APP trafficking and processing to the Alzheimer's plaque peptide amyloid β (Aβ) (Gross *et al*, 2013; Sullivan *et al.*, 2014), although the changes appear to be dependent on specific knockout conditions with both an increase (Kondo *et al*, 2010; Saluja *et al*, 2009; Sano *et al.*, 2006) and decrease (Ho *et al.*, 2008; Sullivan *et al.*, 2014) in Aβ production reported. Thus, the molecular interactions between Mints, synaptic proteins and trafficking partners involved in neurodegenerative diseases is of broad interest to the field.

Mutations in the core neuronal pre-synaptic machinery including Munc18-1 and Sx1a lead to a distinct but overlapping set of neurodevelopmental disorders, with symptoms including neurodevelopmental delay, intellectual disability and early infantile epileptic encephalopathy (Lanoue *et al*, 2019; Verhage & Sorensen, 2020). Mutations in the Mint1-assocated CASK protein have also been found to cause neurodevelopmental disorders with similar features, including mental retardation and microcephaly with ophthalmic atrophy (Hayashi *et al*, 2017; Hsueh, 2009; LaConte *et al*, 2019; Piluso *et al*, 2009), and the human disease linked missense variant p.Leu209Pro in CASK linked to optic nerve hypoplasia specifically disrupts Mint1 binding without impacting other protein interactions (LaConte *et al.*, 2019). Mutations in the Mint proteins themselves have not yet been specifically linked to similar disorders, although copy number variations in Mint2 have been described in patients with epilepsy and intellectual disability (Peycheva *et al*, 2018). In addition, variants in Mint2 have been linked to autism spectrum disorder, potentially through disruption of neurexin trafficking (Babatz *et al*, 2009; Lin *et al*, 2019). By assessing the mechanisms responsible for Mint1 binding to a range of protein partners, we aim to provide a framework that can contribute to the understanding of how Mint1 might modulate a role during neurotransmission and trafficking.

In this work we examined the mechanism of binding between the Mint MID domain and Munc18-1. Using truncations and peptide mutagenesis we defined a minimal acidic short linear interaction motif (SLiM) of thirteen amino acids in Mint1 and Mint2 that is required and sufficient for Munc18-1 interaction. Although phosphorylation in this region of Mint1 can regulate binding to other proteins such as APP, this does not appear to influence Munc18-1 affinity. Using AlphaFold2 we generated a model of the Mint1 and Mint2 sequences bound to Munc18-1 which shows that the peptides form an α-helical structure bound to Munc18-1 at an entirely novel binding site in domain 3b. The binding of this acidic-helical motif (AHM) was extensively validated by mutations in key Mint1 and Munc18-1 residues that disrupt their interaction. Notably the AlphaFold2 model and crystal structure match precisely in all key details. Munc18-1 mutation R388A blocking Mint-1 interaction significantly reduced the number of exocytic events detected using VAMP2-pHluorin unquenching in Munc18-1/2 double knockout PC12 cells. Although the respective Mint1/2 and Sx1a binding sites

in domain 3b and domains 1/3a are distinct from each other, their individual Munc18-1 *in vitro* binding affinities are reduced in the presence of the other ligand. We speculate that this antagonistic allosteric interaction between the two proteins may be important for regulating Munc18-1 templating of SNARE-complex formation. Finally, building on the successful structural predictions of Mint1 with AlphaFold2, we have explored the wider network of interactions mediated by the Mint scaffolds and provide an overall model for its assembly with both effector and regulatory proteins, including the identification of novel binding sites in the Mint PDZ domains for ARF small GTPases and experimental validation of a non-canonical peptide-binding site in the Mint PTB domain that is distinct from the NPxY peptide motif-binding site.

RESULTS

Mapping the Munc18-1-binding sequence of Mint1 and Mint2

A number of studies have shown that both Mint1 and Mint2 homologues can interact with Munc18-1, using methods including immunoprecipitation and yeast two-hybrid assays (Biederer & Sudhof, 2000; Ho *et al*, 2002a; Lee *et al*, 2004; M. Okamoto, 1997; Okamoto & Sudhof, 1997). Mint proteins are multi-domain scaffolds with a C-terminal PTB domain and tandem PDZ domains preceded by a long and unfolded N-terminal sequence that shows low sequence homology across the family (**Fig. 1A; Fig. S1**). Munc18-1 binding has been mapped by yeast two-hybrid assays to a region termed the 'Munc18-interacting domain' (MID) within the N-terminus of the neuronal Mint1 and Mint2 proteins consisting of residues 226-314 and 185-270 respectively (Okamoto & Sudhof, 1997). We first confirmed the direct interaction of Mint1 with purified Munc18-1, performing a GST pull-down assay using the human Mint1 MID as bait (residues 222-314). This showed clear binding between the two proteins that was specific for the neuronal Munc18-1 protein as we did not detect any interaction with Munc18-3 (**Fig. 1B**). As the entire N-terminus of Mint1 including the MID is expected to be unstructured in isolation, we hypothesised that Munc18-1 may be binding to a shorter peptide sequence or SLiM (Diella *et al*, 2008) within the MID. To test this, we generated several truncated Mint1 MID sequences and tested their binding to Munc18-1 by GST pull-down assay (**Fig. 1C**). This showed that a twenty-one amino acid region encompassing residues 261-282 was required and sufficient for Munc18-1 binding.

The binding of a synthetic Mint1 peptide to Munc18-1 was next measured by isothermal titration calorimetry (ITC) and the affinity (K_d) of the interaction was found to be 12.1 ± 1.8 μM (**Fig. 2A, Fig. 2B; Table 1**). With a direct assay for Mint1(261-282) peptide interaction we generated a series of N and C-terminal deletions and found that the minimal binding sequence for Munc18-1 in human Mint1 consists of the thirteen residues from Glu267 to Ser280 (**Fig. 2B**; **Table 1; Fig. S2**). This region is notably the most highly conserved sequence in the N-terminus of Mint1 and Mint2 across species (**Fig. S1**). In line with this we also find that an overlapping peptide from human Mint2 shares a similar binding affinity for Munc18-1 (**Fig. 2B**; **Table 1; Fig. S2**). Within this region the sequence ^{267}EEDIDQIVAE^{276} is invariant across Mint1 and Mint2 homologues from human, fish and xenopus species, although it is not present in worms and flies (**Fig. S1**), and a series of double alanine substitutions in this sequence showed that all these residues are important for Munc18-1 interaction by ITC (**Fig. 2B**; **Table 1; Fig. S2**). The conservation of this minimal binding sequence suggests that Munc18-1 interactions with Mint1 and Mint2 plays a critical role in the functions of these proteins.

We confirmed the binding of Mint1 to endogenous Munc18-1 in PC12 cells by co-immunoprecipitation. GFP-Mint1 or GFP-Mint1(D269A/I270A) were expressed in PC12 cells and bound to GFP-nanotrap beads followed by blotting for the presence of Munc18-1 (**Fig. 2C**). The mutation D269A/I270A reduced Munc18-1 binding in agreement with our *in vitro* ITC data.

149 ***Phosphomimetic Mint1 mutations do not affect the binding to Munc18***

150 The N-terminal region of Mint1 and Mint2 is predicted to be unstructured and can be phosphorylated
151 at numerous sites as catalogued in the PhosphoSitePlus database (Hornbeck *et al*, 2015) (**Fig. S3A**).
152 There are several potential sites of Ser/Thr phosphorylation adjacent to the minimal Munc18-1
153 binding sequences of Mint1 and Mint2 (**Fig. S3B**). Given the overall negative electrostatic charge
154 distribution of the Mint1 and Mint2 N-terminal domains (**Fig. S3C**), we speculated that adding further
155 negative charges in the form of phosphorylation might influence the affinity of the Munc18-1
156 interaction. We designed two longer peptides of Mint1 and Mint2 with putative phosphorylated
157 residues altered to phosphomimetic glutamic acid sidechains and tested their binding by ITC (**Fig.
158 2B**; **Table 1; Fig. S2**). Our results suggest that phosphorylation of Mint proteins near to the Munc18-
159 interacting sequence does not play a direct role in modulating the Munc18-1 binding affinity at least
160 *in vitro*. Previous studies showed that Mint1 and Mint2 N-terminal domains can be phosphorylated
161 upstream of the Munc18-1-interacting sequence by the tyrosine kinase c-Src (Dunning *et al*, 2016).
162 While this enhanced the trafficking of APP via binding the PTB domain, presumably by affecting the
163 overall conformation of Mint1 in some way, it had no effect on Munc18-1 interaction. Phosphorylation
164 of Ser236 and Ser238 in Mint2 also enhance the APP interaction (Sakuma *et al.*, 2009). These sites
165 lie directly adjacent to the Munc18-1-interacting sequence, and our ITC experiments indicate they
166 do not affect Munc18-1 binding (**Fig. 2B**; **Table 1; Fig. S2**). Therefore, it appears that while
167 phosphorylation-dependent conformational changes in the Mint1 N-terminal region play a role in the
168 interactions with APP (and likely other PTB domain-binding transmembrane proteins such as APLP1,
169 APLP2, Megalin and LRP) they are dispensable for Munc18-1 association *in vitro*.

170

171 ***Mint1 forms an acidic α-helical motif that binds to Munc18-1 domain 3b***

172 Despite attempts to crystallise Munc18-1 bound to various Mint1 peptides we were unable determine
173 a high-resolution structure of this complex, including with stabilized Munc18-1 variants (Peleg *et al*,
174 2021). The machine-learning structure-prediction algorithm AlphaFold2 (Evans *et al*, 2022; Jumper
175 *et al*, 2021) has been successfully used to predict structures of protein-peptide complexes by
176 ourselves and others (Ko & Lee, 2021; Poetz *et al*, 2021; Simonetti *et al*, 2021; Tsaban *et al*, 2021).
177 We therefore performed a series of modelling experiments to map the complex between Munc18-1
178 and Mint1 using the ColabFold implementation of AlphaFold2 (Mirdita *et al*, 2022). We initially
179 predicted the complex between the Mint1 and Munc18-1 full-length proteins (**Fig. S4A**). Across
180 multiple models we assessed (i) the prediction confidence measures (pLDDT and interfacial pTM
181 scores), (ii) the plots of the predicted alignment errors (PAE) and (iii) backbone alignments of the
182 final structures. This identified a high-confidence binding sequence in the N-terminal region of Mint1
183 that correlated precisely with the binding motif identified in our biochemical experiments (**Fig. S4A**).

184 Based on this initial model and our biochemical mapping of the minimal Mint1 sequence for
185 Munc18-1 binding we performed multiple independent predictions using a shorter peptide region,
186 combined with AMBER energy minimization to optimize amino acid stereochemistry. We consistently

found that the minimal sequence of Mint1 was predicted to form an extended α-helical structure that associated with the Munc18-1 domain 3b (**Fig. 3A; Fig. 3B**). This novel binding site is highly conserved in Munc18-1 to a similar degree to the binding site for the Sx1a SNARE protein (**Fig. 3C**). In addition, we found that both the human Munc18-1 and Mint2 proteins and the zebrafish Munc18-1 and Mint1 orthologues were consistently predicted to form identical structures (**Fig. S4B, S4C**). In contrast, the human Munc18-3 protein was not predicted to form a stable complex with Mint1 (**Fig. S4D**) consistent with their lack of interaction *in vitro* (**Fig. 1B**). Finally, we modelled the tripartite interaction of human Munc18-1 and CASK with an extended Mint1 sequence containing both the Munc18 and CASK-interacting domain (CID) (**Fig. S4E**). The two Mint1 regions were modelled by AlphaFold2 to bind their respective partners in the expected conformations, with the CASK-binding sequence matching closely in structure to the previous crystal structures of the CASK-Mint complex (Wu *et al.*, 2020; Zhang *et al.*, 2020).

The Mint1 interacting sequence forms what we refer to as an acidic α-helical motif (AHM) as proposed by Li and colleagues (Li *et al*, 2023) (see below), and makes a number of critical contacts with Munc18-1 domain3b including both hydrophobic and electrostatic interactions between conserved sidechains (**Fig. 3D; Movie S1**). Consistent with our truncation and mutation analyses of the Mint1 MID peptides (**Fig. 2B**), all predicted core contacts with Munc18-1 are mediated by Mint1 AHM residues Glu262-Ser280. Towards the N-terminus of Mint1 acidic Glu267, Glu268, Asp269 and Glu276 each form complementary bonds with Munc18-1 residues, most notably with Arg388, Tyr411, and Lys415. These are supported by buried hydrophobic interactions of Mint1 Ile270 and Ile273. On the opposite side of the Mint1 α-helix C-terminus a network of bonds is formed between Mint1 Asp271 and Lys278, with Glu421, Lys425 and His429 of Munc18-1. To confirm the predicted binding site of Mint1 and Mint2 we mutated several residues in domain 3a of Munc18-1 including R388A, L395D, and H429A. In ITC experiments all three mutations showed a reduction in binding affinity and enthalpy, with L395D showing an almost complete loss of association (**Fig. 3E**). Altogether the Mint1 AHM is predicted to form an extensive complementary interface with Munc18-1, and we speculate that the relatively modest affinity between the two proteins may in part be due to the entropic cost of the induced α-helical folding of the AHM sequence.

To test the functional importance of this interaction for Munc18-1 dependent exocytosis in neurosecretory cells, we performed an exocytic release assay using Munc18-1/2 double knockout (DKO) PC12 cell line in rescue conditions (Kasula *et al*, 2019). We measured exocytic events by total internal reflection fluorescence (TIRF) microscopy in DKO-PC12 cells co-transfected with VAMP2-pHluorin and either Munc18-1^{WT}-mEos3.2 or Munc18-1^{R388A}-mEos3.2 – a mutation blocking Mint-1 interaction. VAMP2-pHluorin is classically used to assess vesicular fusion as the intraluminal pH-sensitive pHluorin moiety undergoes unquenching upon exposure to the neutral extracellular environment. This unquenching can be used to study vesicle fusion events and assess the contribution of Munc18-1/Mint1 binding to exocytosis. To assess potential fusion events, we developed a custom Python pipeline that detected puncta of fluorescently labelled vesicles and

assessed them over time. A representative cell shows the initiation and disappearance of several vesicles indicative of fusion events in 3D (time being the 3rd axis) (**Fig. S5**). We found that the cells expressing the Mint1 binding deficient Munc18-1^{R388A}-mEos3.2 showed a reduced number of exocytic events (**Fig. 3F**) and yielded an approximate 40% decrease in the number of evoked exocytic events relative to the level found upon re-expression of the wild-type protein (**Fig. 3G**).

As this work was being completed the Song and Feng labs published similar findings regarding the interaction of Munc18-1 with Mint proteins (Li *et al.*, 2023). The crystal structure of rat Mint1(227-303) bound to a complex of Munc18-1 and Sx1a was solved at 3.2 Å resolution, with electron density observed for Mint1 residues 266-283 associated with Munc18-1 domain 3b. This experimental structure correlates precisely with the region of human Mint1 we have mapped biochemically by truncations and mutagenesis and structurally with AlphaFold2. Based on their crystal structure, Li and colleagues termed the Munc18-1-binding Mint1 sequence the acidic α-helical motif (AHM) and we have also adopted this terminology. Overlay of the Munc18-1/Mint1 crystal structure with our top-ranked AlphaFold2 model shows an essentially identical binding mode in all key details (**Fig. 4A**), and it is important to note the crystal structure was not included in the AlphaFold2 training set. One minor difference is that the AlphaFold2 predictions consistently model stable electrostatic contacts involving Mint1 Glu267 and Glu268. These are not seen in the crystal structure, and this is likely because these electrostatic interactions are relatively transient and thus not clearly observed in the modest resolution electron density maps.

In addition to the crystal structure of Munc18-1/Sx1a bound to the Mint1 AHM, the structure of Munc18-1 was recently determined in a ternary complex with Sx1a and the vesicular R-SNARE VAMP2 (also known as synaptobrevin) by cryoEM (Stepien *et al*, 2022). Similar to what was observed for yeast SM-family protein Vps33, this showed that Munc18-1 can provide a platform to template the assembly of the Qabc-SNARE/R-SNARE complex required for membrane fusion (Baker *et al*, 2015). Overlay of the complexes shows that the Mint1 and VAMP2 binding sites do not overlap and thus Mint1 could potentially associate simultaneously with both SNARE proteins (**Fig. 4B**). However, this does not preclude the possibility that protein dynamics or steric effects of the adjacent vesicle and plasma membranes could affect Mint1 interaction.

Mint1 binding to Munc18-1 allosterically modulates Sx1a interaction

To partly address the question of Munc18-1 dynamics in Mint1 association we examined the effects of domain3a deletions or the presence of Sx1a on their interaction. Previous studies have shown that the flexible hinge-loop region of Munc18-1 domain3a (residues 317-333) is required for efficient priming of secretory vesicles and controls the mobility of Sx1a and subsequent assembly of the SNARE complex (Han *et al*, 2013; Kasula *et al*, 2016; Martin *et al*, 2013). Structural studies of Munc18-1 show that this hinge-loop adopts a ‘closed’ or inhibitory conformation when Munc18-1 is bound to the Sx1a Habc and SNARE domains (Burkhardt *et al*, 2008; Burkhardt *et al*, 2011). Other structures of apo squid Munc18-1, rat Munc18-1 bound to a short Sx1a N-terminal peptide, and the

263 recent cryoEM structure of Munc18-1 in ternary complex with Qa-SNARE Sx1a and R-SNARE
264 VAMP2 show that domain3a can also adopt an 'open' conformation that is thought to be necessary
265 for both releasing Sx1a inhibition and providing a platform for binding and assembly of other SNAREs
266 (Bracher *et al*, 2000; Bracher & Weissenhorn, 2001; Hu *et al*, 2011; Stepien *et al.*, 2022). This is
267 similar to what is seen when yeast SM protein Vps33 is bound to the Nyv1 SNARE (Baker *et al.*,
268 2015). Surprisingly, we find that deletion of the hinge-loop region in Munc18$^{\Delta 317\text{-}333}$, which has only
269 a modest effect on Sx1a binding (Han *et al.*, 2013; Martin *et al.*, 2013), abolishes the binding of Mint1
270 both in GST pull-down and ITC experiments (**Fig. 5A, Fig. 5B**).

271 As Mint1 binds to Munc18-1 domain 3b, we hypothesized that the perturbed Mint1 interaction
272 on deletion of the distal domain 3a hinge-loop might be due to altered structural dynamics in the
273 combined domain3a/3b module. We therefore tested the binding of Sx1a to Munc18-1 in the absence
274 and presence of the Mint1$^{261\text{-}282}$ peptide to determine if there were any changes in Sx1a affinity due
275 to allosteric interactions. By GST pulldown of GST-Mint1 MID we did not observe a gross impact on
276 the ability to bind Munc18-1 in the presence of the high affinity Sx1a ligand (**Fig. 5C**). This is in line
277 with the ability to co-crystallise the three proteins when excess Mint1 is present (Li *et al.*, 2023).
278 However, when we quantified the binding affinity by ITC in the presence of Sx1a in complex with
279 Munc18-1 we saw a small but reproducible reduction in the affinity and enthalpy of binding of
280 Mint1$^{261\text{-}282}$ peptide (**Fig. 5D; Table 2**). In reverse experiments, in the presence of a molar excess of
281 Mint1$^{261\text{-}282}$ peptide we observe a reciprocal reduction in Sx1a binding affinity (K_d) from 7.9 nM to
282 269 nM (**Fig. 5E; Table 2**). This reduced affinity for Sx1a caused by Mint1-dependent allostery is
283 not seen when we use Mint-binding deficient Munc18$^{\Delta 317\text{-}333}$ as expected (**Fig. 5F; Table 2**). Overall,
284 the data indicates that Sx1a and Mint1 binding to Munc18-1 domains 3a and 3b respectively can
285 allosterically regulate the interaction of the other protein. This has potential implications for a role of
286 Mint proteins in Munc18-1 mediated SNARE assembly, which is a tightly regulated and highly
287 dynamic process.

288

289 ***Assessing the network of Mint interactions using AlphaFold2 based predictions***

290 Following the successful modelling of the interaction with Munc18-1/2, we next explored the potential
291 of AlphaFold2 to screen for, and map the binding sites of, other protein-protein interactors of the
292 Mint1 and Mint2 neuronal proteins. Putative Mint1 and Mint2 interactors from the BioGRID repository
293 (Oughtred *et al*, 2021) were screened for direct complex formation with Mint1 and Mint2 respectively
294 using the ColabFold Batch implementation of AlphaFold2 (Mirdita *et al.*, 2022) (**Table S1; Table S2**).
295 To assign a direct 'interactor' from these *in silico* analyses, we used an approach similar to recent
296 work by Sifri and colleagues (Sifri *et al*, 2023). We initially assessed both the AlphaFold2-derived
297 interfacial PTM (iPTM) score and the resultant PAE graphs which provide confidence metrics for the
298 interactions between the proteins. For those with promising scores, we also examined the predicted
299 structures in PyMOL to assess whether interacting regions involved the expected complementary
300 hydrophobic, polar, and electrostatic contacts. To conserve GPU resource allocation, we initially

generated only single predictions of each putative complex in AlphaFold2 in unsupervised batch mode. We found that a minimum iPTM score of ~0.3 combined with a strong signal in the PAE plot for inter-molecular structural correlation typically provided a practical indicator of a complex that was suitable for further assessment. In these cases, we subsequently ran at least three modelling experiments focusing on the specific domains of Mint1/Mint2 and the putative interactors that were predicted to interact with each other, to assess whether multiple predictions resulted in physically plausible structures that consistently aligned with each other in PyMOL (**Table S1; Table S2**).

As expected, these *in silico* interaction screens with AlphaFold2 correctly predicted several well characterized interactors, but they also provided validation of a number of prospective binding partners so far only identified in high-throughput screens (**Figure S6; Figure S7; Table S1; Table S2**). Known interactors include the cytoplasmic NPxY motif of APP (Matos *et al.*, 2012; Xie *et al.*, 2013; Zhang *et al.*, 1997), and the CID sequence of CASK (Wu *et al.*, 2020; Zhang *et al.*, 2020) for which crystal structures have previously been determined. In addition, confident predictions were obtained for several other cytoplasmic sequences of transmembrane proteins previously identified to interact with Mint1 and/or Mint2 including lipoprotein receptors LRP1, LRP2 and LRP8 (Gotthardt *et al.*, 2000; He *et al*, 2007), calsyntenin-1 (CSTN1) (Araki *et al*, 2003) and KCNJ12 (Leonoudakis *et al*, 2004). These all utilize variations of the NPxY motif found in APP to associate with the Mint PTB domains (**Fig. 6**). While LRP1, LRP2 and LRP8 each possess canonical NPxY sequences, CSTN1 and KCNJ12 are predicted to bind the same site of the PTB domain through divergent NPME and NELA sequences respectively. Several other proteins identified in BioGRID were predicted with reasonable confidence to associate directly with Mint1. A putative complex between the homeobox domain of HOXC9 and the PTB domain of Mint1 was modelled by AlphaFold2, via a surface distinct from the NPxY-binding groove. Putative novel interactions between the tandem PDZ domains of Mint1 were also predicted with the USP domain of USP22 (ubiquitin specific peptidase 22) and a C-terminal zinc-finger domain from the large protein WIZ (widely interspaced zinc finger-containing protein).

We chose four predicted interactions to describe in more detail; (i) the association of the Mint1 and Mint2 PTB domains with a peptide sequence from the coiled-coil protein Tight Junction Associated Protein 1 (TJAP1) also called Protein incorporated later into tight junctions (PILT) or tight junction protein 4 (TJP4)) (**Fig 7**), (ii) the association of the Mint1 and Mint2 tandem PDZ domains with ADP-ribosylation factor (ARF) GTPases ARF3 and ARF4 (**Fig. 8A**), (iii) the interactions of the C-terminal sequence of the neurexin-1 (NRX1) receptor with the PDZ2 domain of Mint1/Mint2 (**Fig. 8B**), and (iv) lastly the interaction of an N-terminal YxxΦ motif in Mint1 with the μ3 subunit of the AP3 clathrin adaptor complex (**Fig. 8C**).

Outside of the canonical interactions of NPxY-related motifs with the Mint1 and Mint2 PTB domains, we observed a high confidence complex prediction involving a short peptide sequence in TJAP1 (an interaction only previously reported in high-throughput proteomic screens (Huttlin *et al*, 2021) (**Fig. S7; Table S2**). The TJAP1 binding site is distinct from the binding groove of NPxY motifs,

339 and subsequent predictions of the Mint1 and Mint2 PTB domains in the presence of both the NPxY
340 motif of APP, and the peptide sequence from TJAP1 show highly consistent dual peptide interactions
341 on opposite faces of the PTB domain (**Fig. 7A, B**). Both the APP and TJAP1-binding surfaces of
342 Mint1 and Mint2 are highly conserved (**Fig. 7B**). The binding sequence of TJAP1 encompasses N-
343 terminal residues ^{9}KPYRKAPPEHRELR^{22}, with buried aliphatic sidechains, and complementary
344 electrostatic and hydrogen-bond contacts as shown in **Fig. 7C**. The sequence ^{16}PEHR^{19} is predicted
345 to form a β-turn structure where the Pro16 sidechain forms a stacking interaction with the Arg19
346 guanidino group. To provide further validation of our AlphaFold2 predictions we decided to test the
347 binding of TJAP1 to Mint1 experimentally by ITC. Using the NPxY-containing sequence
348 ^{750}SKMQQNGYENPTYKFFEQMQ^{769} of APP as a positive control we confirmed that this bound to
349 the Mint1 PTB domain with an affinity (K_d) of 0.3 μM (**Fig. 7D; Table 3**), similar to the affinity reported
350 previously (Matos *et al.*, 2012). The TJAP1 peptide ^{9}KPYRKAPPEHRELR^{22} bound to the Mint1 PTB
351 domain with a modest affinity (K_d) of 37 μM (**Fig. 7E; Table 3)**. Importantly, in competition
352 experiments the presence of the APP peptide did not appreciably alter the TJAP1 affinity nor vice
353 versa, confirming that the two peptides interact with distinct sites on Mint1 as predicted (**Fig. 7D and**
354 **7E; Table 3)**. These results show the Mint PTB domains are capable of recruiting proteins via two
355 distinct peptide-motifs.

356 Mint2 was previously identified in a yeast two-hybrid screen for interactors of ARF3 (Hill *et*
357 *al*, 2003). These screens identified fragments of Mint2 containing the tandem C-terminal PDZ
358 domains, and subsequent experiments showed that Mint1, Mint2 and Mint3 could all interact with
359 both ARF3 and ARF4. AlphaFold2 predictions of full-length Mint2 complexed with ARF3 and ARF4
360 revealed a very high confidence interaction of the GTPases with the tandem PDZ domains,
361 correlating with the yeast two-hybrid studies (Hill *et al.*, 2003) (**Fig. S7; Table S2**). Predictions
362 focused on the Mint1 and Mint2 PDZ domains subsequently produced highly consistent complex
363 structures with the two GTPases (**Fig. 8A**). The structure of activated ARF3-GTP bound to a bacterial
364 toxin called MARTX was previously solved by X-ray crystallography (Lee *et al*, 2019). AlphaFold2
365 predicts ARF3 and ARF4 to be in the active GTP-Mg^{2+}-loaded conformation when bound to Mint1,
366 and like the bacterial effector Mint1 and Mint2 primarily engage the switch 2 and interswitch regions
367 of the GTPases, making little contact with the switch 1 region. The ARF GTPases bind an extensive
368 and conserved surface with the interface composed of regions from both PDZ1 and PDZ2 domains
369 in the tandem PDZ structure.

370 Although not listed in the BioGRID entries for Mint1 or Mint2, other studies proposed that
371 their PDZ domains interact with C-terminal sequences of NMDA receptors, kalirin-7, Neurexin-1
372 (NRX1), ApoER2/LRP8 and LDLR (Biederer & Sudhof, 2000; Gotthardt *et al.*, 2000; Jones *et al.*,
373 2014; Minami *et al.*, 2010; Motodate *et al.*, 2019). PDZ domains are small scaffolds that bind to PDZ
374 binding motifs (PDZbms) typically found at the C-terminus of their interacting proteins. They fall in
375 three main classes; Type 1 with consensus [S/T]xΦ (x = any amino acid; Φ = hydrophobic amino
376 acid), Type 2 with consensus ΦxΦ, and Type 3 with consensus [E/D]xΦ .(Hung & Sheng, 2002;

377 Nourry *et al*, 2003). We used AlphaFold2 to predict the interaction of the Mint1 and Mint2 PDZ
378 domains with the C-terminal sequence of NRX1, which conforms to a Type 2 PDZbm. This
379 confidently predicted an interaction between the C-terminal ^{1471}KDKEYYV^{1477} NRX1 sequence with
380 the second PDZ2 domain of the PDZ1-PDZ2 tandem structure (**Fig. 8B**). The C-terminal Val1477
381 side chain (position '0' in standard PDZbm nomenclature) docks in a complementary hydrophobic
382 pocket with the terminal carboxyl group hydrogen bonding with the backbone amides of Mint1
383 Leu759 and Gly760. The NRX1 Tyr1475 and Tyr1476 side chains at positions -1 and -2 pack into
384 complementary surface grooves, while both main-chain and side-hydrogen bonds upstream of the
385 C-terminal interaction provide further specificity. This requires experimental validation, but combined
386 with the fact that the C-terminal Mint1 sequence PVYI (PLIY in Mint2) itself can form an
387 intramolecular interaction with its own PDZ1 domain (Long *et al*, 2005) it suggests that the PDZ2
388 domain of the Mint proteins provides the major platform for recruiting PDZbm-containing ligands.

389 The last predicted interaction we examined in detail was that of Mint1 with the μ3 subunit of
390 the tetrameric AP3 clathrin adaptor complex (**Fig. 8C**), another unexpected association reported in
391 the same high-throughput screens as TJAP1 (Huttlin *et al.*, 2021). The μ3 subunit has an N-terminal
392 longin domain that embeds it within the AP3 tetramer, and a C-terminal μ-homology domain (MHD)
393 that associates with YxxΦ tyrosine-based motifs (where Φ is a bulky hydrophobic residue), typically
394 in transmembrane cargos for sorting from endosomes to lysosomal compartments (Mardones *et al*,
395 2013; Sanger *et al*, 2019). The predicted structure of the Mint1 ^{298}YEEI^{301} sequence closely
396 resembles the crystal structure of the TGN38 motif YQRL bound to the rat μ3 MHD, with both Tyr298
397 and Ile301 inserting into complementary surface pockets as typically seen for YxxΦ motifs. We also
398 tested AlphaFold2 predictions of the Mint1 sequence with other μ-subunits from AP1, AP2, AP4 and
399 AP5. While μ1, μ2 and μ4 proteins were each predicted to interact, the iPTM confidence scores were
400 much lower, and AP5 was not predicted to bind at all.

401 While we have focused on proteins that *are* predicted to bind to Mint1/Mint2, it is notable that
402 from the list of putative BioGRID interactors the majority are *not* predicted to associate directly with
403 the Mint adaptors, including many that have previously been identified using methods such as co-
404 immunoprecipitations (**Table S1; Table S2**). In some case this could be due to limitations with the
405 predictive ability of AlphaFold2. However, it likely indicates that many of the proteins reported in
406 BioGRID either bind indirectly (via other proteins not included in our binary predictions) or are non-
407 specific interactions detected by the proteomics methods.

408 **DISCUSSION**

409 The interaction of Munc18-1 with Mint proteins has long been known to be important for synaptic
410 neurotransmitter and hormonal release through the regulation of SNARE-mediated vesicle fusion.
411 While the molecular basis for the scaffolding and trafficking of the APP transmembrane protein and
412 CASK kinase have been structurally characterised (Matos *et al.*, 2012; Wu *et al.*, 2020; Xie *et al.*,
413 2013; Zhang *et al.*, 1997; Zhang *et al.*, 2020), the mechanism by which Mint bind to Munc18-1 was
414 unknown. In this work, and in a recent study by Li and colleagues (Li *et al.*, 2023), the interaction is
415 revealed to be via the binding of Munc18-1 domain3b via a conserved α-helical motif (AHM) in the
416 N-terminal unstructured domains of the Mint1 and Mint2 neuronal homologues. The binding surface
417 on Munc18-1 is distinct from its known binding sites for the Sx1a and VAMP2 SNARE proteins,
418 although we find there is a small but significant reduction in the binding affinity of Sx1a in the
419 presence of the Mint1 AHM. In line with a role for the Mint1 interaction in Munc18-1-dependent
420 exocytosis we observed that perturbation of Munc18-1 Mint-1 interaction in domain 3b impacted
421 exocytosis in neurosecretory cells. We speculate this could point to a role of Mint proteins in
422 regulating the SNARE complex dynamic templating activity of Munc18-1 which will be worth future
423 investigation.

424 The AHM sequence found in Mint1 and Mint2 is conserved across many species, although it
425 appears not to be present in some organisms such as nematodes and flies. Further, it may be
426 relatively specific to the Mint proteins, with few if any other proteins possessing similar motifs. We
427 scanned the human genome using ScanProsite and did not find any other proteins with highly similar
428 sequences. Li and colleagues reported potential AHMs in Munc13-1, Bassoon, and Atg16L, although
429 no binding was detected using the putative motif from Munc13-1 by ITC (Li *et al.*, 2023). Future
430 proteomic studies of Munc18-1 using specific domain3b mutations may reveal the existence of other
431 proteins able to bind this site, but there are unlikely to be a large number. Like the CASK-binding
432 CID sequence in Mint1, the Mint1 and Mint2 AHM sequences lie within their extended and
433 intrinsically unstructured N-terminal domain, likely adopting their α-helical structures via induced
434 folding upon Munc18-1 interaction. This may explain the relatively modest binding affinity for
435 Munc18-1 despite the reasonably large binding surface. The interaction between these proteins is
436 thus likely highly context dependent, relying on both their specific coupling as well as their
437 colocalization at the membrane surface and likely clustering with other proteins such as the SNAREs,
438 APP, neurexins, and potentially small GTPases like ARF3.

439 In addition to dissecting the mechanism of Mint1 and Mint2 interaction with Munc18-1, we
440 have used machine learning-based structure prediction with AlphaFold2 to assess the broader
441 interactome of the Mint proteins. These predictions provide useful insights into those interactions
442 that are likely to be directly mediated by the Mint proteins, as validated at least in one instance with
443 the direct binding of TJAP1 confirmed. Our results thus provide an example of how AlphaFold2 (and
444 similar algorithms) can be used to provide confidence in the plausibility of complexes identified in
445 larger proteomic datasets (Burke *et al*, 2023; Gao *et al*, 2022a; Gao *et al*, 2022b; Humphreys *et al*,

2021; Sifri *et al.*, 2023; Yu *et al*, 2023). Such an approach has the potential to inform and accelerate subsequent experimental validation of molecular complexes detected in high-throughput screens, by providing much greater confidence as to which hits represent specific interactions.

Apart from the expected predictions of CASK and APP, for which previous crystal structures are available, there were several other notable complexes that were confidently modelled by AlphaFold2 in this study. A number of proteins have been reported to interact with the PDZ domains of Mint1 and Mint2 via C-terminal PDZbms, including calcium channels (Maximov *et al*, 1999), kalirin-7 (Jones *et al.*, 2014; Penzes, 2001), NMDA receptors (Motodate *et al.*, 2019) and NRX1 (Biederer & Sudhof, 2000; Dean & Dresbach, 2006). Furthermore, the C-terminus of Mint proteins can form an intramolecular interaction with the PDZ1 domain, effectively acting as an autoinhibitory sequence of PDZ1 (Long *et al.*, 2005). Taking NRX1 as an example, we found that its Type II PDZbm was predicted to interact with the PDZ2 domain in the canonical β-strand orientation, and since other neurexin homologues share the same C-terminal sequence they likely use the same binding mechanism. This hypothesis, as well as whether the second PDZ2 domain is bound by other PDZbms warrants further investigation.

One novel Mint interactor predicted by AlphaFold2 and validated in direct binding experiments was TJAP1, which was previously identified in high-throughput proteomic screens with all three Mint homologues (Huttlin *et al.*, 2021). TJAP1 has an N-terminal unstructured region, which we predicted to interact with Mint PTB domains, a central-coil region predicted by AlphaFold2 to form a homodimer (not shown), and an extended C-terminal unstructured and Proline-rich domain. The precise function of TJAP1 is essentially unknown, although it was identified in yeast two-hybrid assays to bind the GTPase ARF6 (Tamaki *et al*, 2012) and discs large-2 (Dlg-2/PSD93) (Kawabe *et al*, 2001), a member of the membrane-associated guanylate kinase (MAGUK) protein family that includes CASK (Ye *et al*, 2018). TJAP1 is localised to both the Golgi and tight junctions (Kawabe *et al.*, 2001; Tamaki *et al.*, 2012), and the putative interaction with the TJAP1 N-terminal peptide sequence is confidently predicted with not only the neuronal Mint1 and Mint2 proteins but also the ubiquitous Mint3 protein (not shown) so it is possible that the association is important in cell types other than neurons.

Similar to TJAP1, the ARF3 and ARF4 small GTPases were originally identified to bind Mint proteins in yeast two-hybrid screens (Hill *et al.*, 2003), however no subsequent studies have examined the mechanism or functional role of these interactions. Our modelling indicates a conserved binding site involving the PDZ1 and PDZ2 tandem domains of the Mint proteins, which support the original yeast two-hybrid mapping experiments. ARF3 is highly enriched in the brain, and both proteins play a role in maintaining recycling endosome morphology and integrity (Kondo *et al*, 2012; Nakai *et al*, 2013). Interestingly ARF3 mutations have recently been found in patients with neurodevelopmental disorders characterised by brain abnormalities, microcephaly and seizures (Fasano *et al*, 2022; Sakamoto *et al*, 2021). It is tempting to speculate these disorders overlap with synaptic pathologies caused by mutations in Munc18-1, CASK and other synaptic proteins, thus

484 suggesting a role for ARF3 in the synaptic vesicle trafficking pathways that could in part be mediated
485 through the Mint proteins.

486 The last predicted interaction we examined was that of Mint1 with the AP3 clathrin adaptor
487 complex. This involves binding of the AP3 μ3A domain with a canonical YxxΦ sequence in the Mint1
488 N-terminal region (not present in Mint2 or Mint3). It would indicate that the Mint1 N-terminus has at
489 least two functions distinct from the other Mint isoforms; the ability to bind CASK, and the potential
490 to couple Mint1 and bound proteins (such as APP or neurexins for example) into AP3 mediated
491 transport structures. AP3 is primarily found on endosomes where it mediates trafficking to lysosomes
492 and lysosome-related organelles (Sanger *et al.*, 2019), and depending on specific subunit isoforms
493 has important roles in axonal transport and synaptic function by regulating the reformation of synaptic
494 vesicles from endosomes derived from bulk synaptic endocytosis (Blumstein *et al*, 2001; Evstratova
495 *et al*, 2014; Li *et al*, 2016; Newell-Litwa *et al*, 2010; Seong *et al*, 2005; Shetty *et al*, 2013; Voglmaier
496 *et al*, 2006). Similar to ARF3, mutations in neuronal AP3 isoforms can lead to neurodevelopmental
497 disorders with some similar features to synaptopathies (Lanoue *et al.*, 2019), suggesting a potential
498 functional overlap of Mint1 and AP3 in synaptic integrity (Ammann *et al*, 2016; Assoum *et al*, 2016).

499 An overall model for Mint1 is shown in **Fig. 9** summarising the known and predicted
500 interactions mediated by this scaffold protein. **Fig. 9A** shows an AlphaFold2 prediction of the full-
501 length protein highlighting binding sequences and structural domains of the protein and underlines
502 the highly extended nature of the N-terminal intrinsically disordered domain containing the Munc18-
503 1 binding AHM as well as binding motifs for the AP3 adaptor and CASK. **Fig. 9B** is a cartoon
504 summary of the interactions described above and highlights the overall scaffolding function of this
505 protein. From our biophysical and biochemical studies, we speculate that the reduced affinity of Sx1a
506 for Munc18-1 in the presence of the Mint AHM sequence could lead to an enhancement of SNARE
507 assembly mediated by Munc18-1 templating, although this will require further validation. A final
508 caveat to this model is that it does not account for temporal regulation of the various interactions,
509 the impact of posttranslational modifications or the cellular context where each interaction is likely to
510 occur including the plasma membrane and other organelles such as endosomes and the Golgi.

511 In summary, we have mapped and characterised the specific association of the neuronal
512 Mint1 and Mint2 proteins with the SNARE regulatory protein Munc18-1 providing a high-resolution
513 snapshot for how these key synaptic proteins interact with other, confirming and extending recent
514 related work (Li *et al.*, 2023). This study further emphasises the ability of AlphaFold2, at least in
515 many instances, to predict protein-peptide interactions with a high degree of accuracy. By applying
516 a wider set of systematic analyses, our work has revealed likely modes of interaction between the
517 Mint proteins and a variety of known and novel effectors, which provides a foundation for future
518 mechanistic studies of their important role in synaptic activity.

519

520 **METHODS**

521 ***Antibodies, plasmids and peptides***

522 Human Mint1 sequences for bacterial expression were codon optimised and sub-cloned into the
523 pGEX4T-2 plasmid by Genscript (USA). The constructs generated were GST-tagged Mint1(226-
524 314)(MID), Mint1(261-272), Mint1(261-282), Mint1(226-289), Mint1(222-314), Mint1(237-289).
525 Human Mint1 open reading frame and mutant Mint1(D269A/I270A) were obtained from Genscript
526 and cloned into the pcDNA3.1-N-eGFP. The human Mint1 PTB domain (residues 448-623)
527 sequence was synthesised and cloned into pGEX6P-2 by Gene Universal.

528 All Mint-derived synthetic peptides were purchased from Genscript (USA). The human
529 APP(750-769) (SKMQQNGYENPTYKFFEQMQ) and TJAP1(9-22) (KPYRKAPPEHRELR) peptides
530 were made by solid phase peptide synthesis in-house, purified by reverse phase HPLC and purity
531 assessed by mass spectrometry. GFP polyclonal antibody and Goat anti-mouse secondary antibody
532 were purchased from Thermo Fisher and Mouse monoclonal anti-munc18-1 was purchased from
533 BD biosciences. pmEos3.2-N1 Munc18-1^{WT} was created by restriction digestion of Munc18-1^{WT}
534 (double digestion with NheI/AgeI, New England Biosciences) from pmEos2-N1 Munc18-1^{WT} (Kasula
535 et al. 2015 *Journal of Cell Biology*), vector linearisation of pmEos3.2-N1 with NheI/AgeI was followed
536 by T4 Ligation. pmEos3.2-N1 Munc18-1^{WT} was then used as a template to introduce the following
537 missense mutation R388A using Quick-Change Lightning site-directed mutagenesis kit (Agilent
538 Technologies, Cat# 210518) as per manufacturer's instructions. Primers were designed by PrimerX
539 (site: http://bioinformatics.org/primerx/) and ordered from SigmaAldrich. M18-1_R388A_For: 5'
540 GAAAAAATCAAGGACCCCATGGCAGCCATTGTCCCCATCCTGC 3' and M18-1_R388A_Rev: 5'
541 GCAGGATGGGGACAATGGCTGCCATGGGGTCCTTGATTTTTTC 3'. All new plasmids were
542 verified by sanger sequencing performed by the Australian Genome Resource Facility (Brisbane,
543 Australia). pCI VAMP2-pHluorin was a kind gift from James Rothman (Miesenbock *et al*, 1998).

544

545 ***Recombinant protein expression and purification***

546 All proteins were expressed in *Escherichia coli* Rosetta™(DE3) cells. GST-Mint1 (226-314, the
547 Munc18-1 interacting domain (MID)), containing pGEX4T-2 vector was transformed into Rosetta
548 cells and plated on a LB/Agar plate supplemented with Ampicillin (0.1mg/mL). Single colony was
549 then used to inoculate 50 mL of LB medium containing Ampicillin (0.1 mg/mL). and the culture was
550 grown overnight at 37 ^{o}C with shaking at 180 rpm. The following day, 1L of LB medium containing
551 antibiotics Ampicillin (0.1 mg/mL) and Chloramphenicol (0.034 mg/mL) was inoculated using 10 mL
552 of the overnight culture. Cells were then grown at 37 ^{o}C with shaking at 180 rpm to an optical density
553 of 0.7-0.8 at 600 nm and the protein expression was induced by adding 0.5 mM IPTG (isopropyl-β-
554 D-thiogalactopyranoside). Expression cultures were incubated at 20 ^{o}C overnight. And the cells were
555 harvested next day by centrifugation at 4000 rpm for 15 min using Beckman rotor JLA 8.100. Cell
556 pellets were resuspended in 20 mL (for cell pellet from 1L) of lysis buffer (50 mM Tris, pH 8.0, 500
557 mM NaCl, 10% glycerol, 1 mM DTT, Benzamidine (0.1mg/mL), and Dnase (0.1 mg/mL)).

558 Resuspended cells were further lysed by using the cell disrupter (Constant systems, LTD, UK , TS-
559 Series) and the soluble fraction containing GST-Mint1 was separated from cell debris by
560 centrifugation at 18,000 rpm for 30 min at 4 °C. The soluble fraction was first purified by affinity
561 chromatography using glutathione-Sepharose resin and the GST-Mint1 was eluted using 50 mM Tris,
562 pH 8.0, 500 mM NaCl, 10% glycerol, 1 mM DTT buffer and the protein containing fractions were
563 concentrated and further purified by gel filtration chromatography (Superdex 75 (16/600), GE
564 Healthcare). GST-Mint1 containing fractions were analysed by SDS PAGE. All the other GST-Mint1
565 N-terminal constructs (GST-Mint1 261-272, 261-282, 226-289, 222-314, 237-289) were also
566 expressed and purified as described above. The GST-Mint1 PTB domain was expressed as above,
567 but the GST tag was removed by incubation with Prescission protease, followed by gel filtration into
568 50 mM HEPES, 200 mM NaCl, 0.5 mM TCEP and 5% glycerol.
569 For GFP-nanotrap preparation, the plasmid pOPINE harbouring His-SUMO-GFP-nanotrap
570 was transformed into *Escherichia coli* Bl21 (DE3) cells and plated on a LB/Agar plate supplemented
571 with Ampicillin. GFP-nanotrap refers to the camelid-derived nanobody specific for GFP (Kubala *et*
572 *al*, 2010). The expression and lysis of cells were carried out as described above. The supernatant
573 containing GFP nano trap was first purified by affinity chromatography using Talon resin equilibrated
574 with 50 mM Tris (pH 8.0), 500 mM NaCl, 10 % Glycerol and protein bound to the column was eluted
575 using elution buffer containing 50 mM Tris (pH 8.0), 500 mM NaCl, 10 % Glycerol, 300 mM Imidazole.
576 The fractions containing GFP-nanotrap was combined, concentrated and loaded on to a Superdex
577 75 (16/60) column equilibrated with 50 mM Hepes (pH 7.5), 200 mM NaCl, 0.5 mM TCEP (tris(2-
578 carboxyethyl)phosphine). The fractions containing the protein were analysed by SDS PAGE,
579 combined, and concentrated to the desired concentration. Rat Sx1a ($Sx1_{1-261}$-His), Munc18-1-His
580 and Munc18-$1^{\Delta 317-333}$ were also expressed and purified to homogeneity as described Hu et al (Hu *et*
581 *al.*, 2011).
582
583 ***Cell culture and Transfection:***
584 Neurosecretory cell line, Pheochromocytoma cells (PC12) and Munc18-1/ 2 double knockout PC12
585 cells (DKO-PC12) (Kasula *et al.*, 2019), were cultured at 37 °C/5% CO_2 in normal culture media
586 (Dulbecco's modified Eagle's medium (High glucose, pyruvate, Gibco, Cat#11995), 7.2% Heat-
587 inactivated Foetal Bovine Serum (Gibco), 7.2% Heat-inactivated Horse Serum (Gibco), 1x
588 GlutaMAX™ supplement (Gibco, Cat# 35050061)). Cells were transfected using Lipofectamine™
589 LTX (Invitrogen, Cat#15338100) as per manufacturer's instructions. For co-IP experiments PC12
590 cells 4 x 10^6 cells were cultured in 10 cm culture dishes (TPP Techno Plastic Products AG) coated
591 with 0.1 mg/mL Poly-D-Lysine (Sigma, P2636). For each condition 15.3 μg plasmid DNA was used
592 per 10 cm dish and 2x 10 cm dishes were pooled for experiments. PC12 cells were transfected with
593 either pEGFP-N1 (GFP Control), pcDNA3.1-N-eGFP hMint1 WT or pcDNA3.1-N-eGFP hMint1
594 DI/AA mutant, and 48hr post transfected cell pellets were collected for subsequent co-IP/GFP Trap.

595 Munc18 DKO-PC12 cells were co-transfected with 1 µg pCI VAMP2-pHluorin and 1 µg of either
596 pmEos3.2-N1 Munc18-1WT or pmEos3.2-N1 Munc18-1 R388A with 6.75 µL Lipofectamine™ LTX
597 with PLUS Reagent™ (ThermoFisher, Cat# 15338-100) into 3.5 cm petri dishes as per the
598 manufacturer's instructions. Cells were re-plated after 24 h onto 0.1 mg/mL Poly-D-Lysine
599 (SigmaAldrich, Cat#P2636-100MG) coated glass-bottom petri-dishes (Cellvis, Cat# D29-20-1.5-N)
600 and imaged 48 hrs after transfection.
601
602 ***Co-immunoprecipitation (Co-IP)***
603 PC12 cells containing EGFP, GFP- hMint1 (WT), GFP hMint1 DI/AA were lysed on ice using buffer
604 composed of 20 mM Hepes, 50 mM NaCl, 1% Triton, 1 mM DTT, DNAse and a tablet of protease
605 inhibitor cocktail. To further enhance the Lysis, the lysate was aspirated through a small needle
606 approximately 10 times. The lysate was then centrifuged at 17,000 *g* for 15 minutes to separate the
607 cellular debris from the supernatant containing the soluble proteins. 50 μl of GFP nano trap coupled
608 to NHS activated Sepharose 4 beads were added to each of the three supernatants containing GFP,
609 GFP-hMint1 WT and GFP-hMint1 DI/AA. The supernatant-bead mixtures were incubated for 2 hours
610 at 4 °C while shaking, and then the beads were spun down by at 5000 *g* for 2 minutes to remove the
611 unbound proteins. The bead samples were washed three times using the lysis buffer, and 50 μl of
612 SDS sample buffer was added to each sample. The beads, containing the immunoprecipitated
613 proteins were boiled at 95 °C for 5 minutes to elute the bound proteins and resolved using Western
614 immunoblotting. GFP and Munc18a proteins were detected using anti-GFP mouse and anti-
615 Munc18a mouse as primary antibodies respectively and Goat anti-mouse antibody as the secondary
616 antibody. The final imaging was performed using ECL and Odyssey infrared imaging system (LI-
617 COR).
618
619 **Total Internal Reflection Fluorescence Microscopy (TIRFM) and cell footprint analysis**
620 For live cell TIRF imaging, transfected Munc18 DKO-PC12 cells were imaged in glass-bottom dishes
621 bathed in Buffer A (145 mM NaCl, 5 mM KCl, 1.2 mM Na_2HPO_4, 10 mM D-glucose, 20 mM HEPES,
622 pH 7.4) and imaged immediately before and following 2 mM $BaCl_2$ addition, to elicit vesicle fusion
623 (Papadopulos *et al*, 2013). Dishes were imaged on an iLas2 Microscope (Roper Scientific) equipped
624 with a Nikon CFI Apo TIRF 100×/1.49 NA oil-immersion objective, and an Evolve 512 Delta EMCCD
625 camera (Photometrics) and Metamorph Imaging Software version 7.7.8. Cells were imaged at 10 Hz
626 (100 ms acquisition), for 3000 frames (300 seconds) at 37°C/5% CO_2, and 30% of the initial 491
627 laser power in TIRF.
628
629 **Vesicle Fusion Assays in Munc18 DKO cells**
630 To assess vesicle fluorescence over time a custom Python 3.8 pipeline was developed. For a typical
631 3000 frame TIRF acquisition, the data was read into a Python z-stack and divided into 100 frame
632 intervals. The fluorescence at each interval was averaged, and fluorescent puncta identified at pixel

633 resolution (where 1 pixel = 106 nm) using the Laplacian of Gaussian functionality of Python OpenCV.
634 The puncta were used to populate a 3D [x,y,t] array. 3D DBSCAN (scikit-learn) was used to identify
635 clusters of puncta which were within 1 pixel spatially and 2 pixels temporally. The time corresponding
636 to the disappearance of each cluster was used as the indicator of a completed fusion event. Ongoing
637 clusters that had not disappeared by the end of the acquisition were not considered for further
638 analysis.
639
640 **Statistical Analysis of vesicle fusion events in Munc18 DKO cells**
641 Unless otherwise stated, values are represented as mean±SEM. The tests used for statistical
642 analysis are indicated in the respective figure legends. Non-parametric Mann Whitney U test was
643 used to compare two groups of for non-normally distributed data. Comparisons of the same cells
644 analysed before and after stimulation was analysed by a paired statistical test. Data were considered
645 significant at $P < 0.05$.
646
647 ***Isothermal titration calorimetry (ITC)***
648 For ITC, all peptides were weighed and initially dissolved in the working buffer to make a stock
649 concentration of 2 mM. ITC experiments measuring Munc18-1 binding to Mint1 peptides and Sx1a
650 were carried out on Microcal iTC200 at 25°C. GST-Mint1 and all the other proteins used in the
651 experiments were buffer exchanged into 50 mM Tris, (pH 8.0), 200 mM NaCl by gel filtration prior to
652 ITC. GST-Mint1 (1 mM), Sx1a (1 mM) or Mint1 synthetic peptide (0.7 mM) were titrated into Munc18-
653 1-His (50 μM). Mint1 PTB domain binding to the APP and TJAP1 peptides was performed in 50 mM
654 HEPES, 200 mM NaCl, 0.5 mM TCEP and 5% glycerol at 25°C with 1 mM peptides titrated into 50
655 μM Mint1 PTB domain. The binding parameters, equilibrium constant K_a ($1/K_d$), stoichiometry (n)
656 and the enthalpy (ΔH) were determined by processing the ITC data using ORIGIN 7.0 software. The
657 equation, $\Delta G = \Delta H - T\Delta S$ was used to calculate the Gibbs free energy (ΔG) and all the experiments
658 were performed in triplicate to calculate the standard error of the mean (SEM) for thermodynamic
659 parameters.
660
661 ***Pull down assays***
662 Pull down assays were carried out using GST-Mint1 and Munc18-1-His. 0.5 nmol of GST-Mint1 was
663 mixed with 1 nmol of Munc18-1-His in 500 μL of pull down buffer (50 mM Tris pH 8.0, 200 mM NaCl,
664 1mM DTT, 0.1% IGEPAL) and incubated for 30 min on a rotating holder at 4 ^{o}C. The protein mixture
665 was then centrifuged at full speed for 5 min and 50 μL of glutathione Sepharose resin pre-equilibrated
666 in pull down buffer was added. The protein mix with the resin was incubated further 30 min at 4 ^{o}C
667 on a rotating holder and at the end of the incubation, the beads were spun down at 5000 rpm for 30
668 sec. The supernatant containing the unbound protein is pipetted off and the beads with the bound
669 protein was washed 4 times with 1 mL of pull down buffer. 50 μL of SDS sample buffer was added
670 to the beads and analysed by SDS-PAGE for bound proteins.

671

672 ***Protein structural prediction, modelling and visualisation***

673 All protein models were generated using AlphaFold2 Multimer (Evans *et al.*, 2022; Jumper *et al.*,
674 2021) implemented in the Colabfold interface available on the Google Colab platform (Mirdita *et al.*,
675 2022). For each modelling experiment ColabFold was executed using default settings where multiple
676 sequence alignments were generated with MMseqs2 (Mirdita *et al*, 2019). For all final models
677 displayed in this manuscript, structural relaxation of peptide geometry was performed with AMBER
678 (Hornak *et al*, 2006). For all modelling experiments, we assessed (i) the prediction confidence
679 measures (pLDDT and interfacial iPTM scores), (ii) the plots of the predicted alignment errors (PAE)
680 and (iii) backbone alignments of the final structures. For modelling of the complex between Munc18-
681 1 and Mint1 we initially predicted the complex between full-length proteins and identified a high-
682 confidence binding sequence in the N-terminal region of Mint1 that correlated precisely with the
683 binding motif identified in our biochemical experiments. Based on this initial model and our
684 biochemical mapping of the minimal Mint1 sequence for Munc18-1 binding we performed multiple
685 independent predictions using a shorter peptide region, combined with AMBER energy minimization
686 to optimize amino acid stereochemistry.

687 For interactome-wide analysis of other protein-protein interactors of Mint1 and Mint2 we
688 obtained a list of putative interactors from the BioGRID repository (Oughtred *et al.*, 2021), and
689 predicted whether they formed direct complexes using the ColabFold Batch implementation of
690 AlphaFold2 (Mirdita *et al.*, 2022) (**Table S1; Table S2**). To assign a direct 'interactor' from these *in*
691 *silico* analyses we used an approach similar to recent work by Sifri and colleagues (Sifri *et al.*, 2023).
692 We initially assessed both the AlphaFold2-derived interfacial PTM (iPTM) score and the resultant
693 PAE graphs which provide confidence metrics for the interactions between the proteins. For those
694 with promising scores we also examined the predicted structures in PyMOL to assess whether
695 interacting regions involved the expected complementary hydrophobic, polar, and electrostatic
696 contacts. To conserve GPU resource allocation, we initially generated only single predictions of each
697 putative complex in AlphaFold2 in unsupervised batch mode. We found that a minimum iPTM score
698 of ~0.3 combined with a strong signal in the PAE plot for inter-molecular structural correlation
699 typically provided a useful indicator of a complex that was suitable for further assessment. In these
700 cases, we subsequently ran at least three modelling experiments focusing on the specific domains
701 of Mint1/Mint2 and the putative interactors that were predicted to interact with each other, to assess
702 whether multiple predictions resulted in physically plausible structures that consistently aligned with
703 each other in PyMOL (**Table S1; Table S2**). Sequence conservation across PDB models was
704 mapped with Consurf (Ashkenazy *et al*, 2016). All structural images were made with Pymol
705 (Schrodinger, USA; https://pymol.org/2/).

706

Acknowledgements

This work was supported by grants from the National Health and Medical Research Council of Australia (NHMRC) (APP1138083 and APP1139316) to B.M.C and FAM. B.M.C is supported by an NHMRC Investigator Grant and previous Senior Research Fellowship (APP2016410 and APP1136021). F.A.M is supported by an NHMRC Senior Research Fellowship (GNT1155794). T.P.W is supported by an NHMRC Ideas Grant (APP2010901) awarded to T.P.W and F.A.M. We would like to thank Lionel Louiset, Ailisa Blum, Pranesh Padmanabhan and Jenny Martin for their assistance with this work, including initial mammalian construct testing, funding contributions and supervision of students.

Author contributions

B.M.C. designed research with some input of F.A.M; S.W. and E.L. performed ITC analysis, pulldown assays and S.W. and B.M.C. performed AlphaFold2 modelling; S.W. and R.S.G performed the coimmunoprecipitation assays. R.S.G performed cell culture, plasmid design and cloning; A.M performed site directed mutagenesis with the help of R.S.G., cell culture and TIRFM with the help of A.T.B.. T.P.W designed the exocytic fusion assay Python pipeline and performed the analysis. A.J assisted with data processing and analysis. F.A.M. and B.M.C acquired funding and provided student supervision; and S.W., R.S.G., F.A.M. and B.M.C wrote the paper with input by all authors.

Conflict of interest

Authors declare that they have no conflict of interest.

References

Ammann S, Schulz A, Krageloh-Mann I, Dieckmann NM, Niethammer K, Fuchs S, Eckl KM, Plank R, Werner R, Altmuller J *et al* (2016) Mutations in AP3D1 associated with immunodeficiency and seizures define a new type of Hermansky-Pudlak syndrome. *Blood* 127: 997-1006

Araki Y, Tomita S, Yamaguchi H, Miyagi N, Sumioka A, Kirino Y, Suzuki T (2003) Novel cadherin-related membrane proteins, Alcadeins, enhance the X11-like protein-mediated stabilization of amyloid beta-protein precursor metabolism. *J Biol Chem* 278: 49448-49458

Ashkenazy H, Abadi S, Martz E, Chay O, Mayrose I, Pupko T, Ben-Tal N (2016) ConSurf 2016: an improved methodology to estimate and visualize evolutionary conservation in macromolecules. *Nucleic Acids Res* 44: W344-350

Assoum M, Philippe C, Isidor B, Perrin L, Makrythanasis P, Sondheimer N, Paris C, Douglas J, Lesca G, Antonarakis S *et al* (2016) Autosomal-Recessive Mutations in AP3B2, Adaptor-Related Protein Complex 3 Beta 2 Subunit, Cause an Early-Onset Epileptic Encephalopathy with Optic Atrophy. *Am J Hum Genet* 99: 1368-1376

Babatz TD, Kumar RA, Sudi J, Dobyns WB, Christian SL (2009) Copy number and sequence variants implicate APBA2 as an autism candidate gene. *Autism Res* 2: 359-364

Baker RW, Jeffrey PD, Zick M, Phillips BP, Wickner WT, Hughson FM (2015) A direct role for the Sec1/Munc18-family protein Vps33 as a template for SNARE assembly. *Science* 349: 1111-1114

Becamel C, Alonso G, Galeotti N, Demey E, Jouin P, Ullmer C, Dumuis A, Bockaert J, Marin P (2002) Synaptic multiprotein complexes associated with 5-HT(2C) receptors: a proteomic approach. *EMBO J* 21: 2332-2342

Biederer T, Cao X, Sudhof TC, Liu X (2002) Regulation of APP-dependent transcription complexes by Mint/X11s: differential functions of Mint isoforms. *J Neurosci* 22: 7340-7351

Biederer T, Sudhof TC (2000) Mints as adaptors. Direct binding to neurexins and recruitment of munc18. *J Biol Chem* 275: 39803-39806

Blumstein J, Faundez V, Nakatsu F, Saito T, Ohno H, Kelly RB (2001) The neuronal form of adaptor protein-3 is required for synaptic vesicle formation from endosomes. *J Neurosci* 21: 8034-8042

Borg JP, Ooi J, Levy E, Margolis B (1996) The phosphotyrosine interaction domains of X11 and FE65 bind to distinct sites on the YENPTY motif of amyloid precursor protein. *Mol Cell Biol* 16: 6229-6241

Borg JP, Straight SW, Kaech SM, de Taddeo-Borg M, Kroon DE, Karnak D, Turner RS, Kim SK, Margolis B (1998) Identification of an evolutionarily conserved heterotrimeric protein complex involved in protein targeting. *J Biol Chem* 273: 31633-31636

Bracher A, Perrakis A, Dresbach T, Betz H, Weissenhorn W (2000) The X-ray crystal structure of neuronal Sec1 from squid sheds new light on the role of this protein in exocytosis. *Struct Fold Des* 8: 685-694

Bracher A, Weissenhorn W (2001) Crystal structures of neuronal squid Sec1 implicate inter-domain hinge movement in the release of t-SNAREs. *J Mol Biol* 306: 7-13

Burke DF, Bryant P, Barrio-Hernandez I, Memon D, Pozzati G, Shenoy A, Zhu W, Dunham AS, Albanese P, Keller A *et al* (2023) Towards a structurally resolved human protein interaction network. *Nat Struct Mol Biol*

773 Burkhardt P, Hattendorf DA, Weis WI, Fasshauer D (2008) Munc18a controls SNARE assembly
774 through its interaction with the syntaxin N-peptide. *EMBO J* 27: 923-933

775 Burkhardt P, Stegmann CM, Cooper B, Kloepper TH, Imig C, Varoqueaux F, Wahl MC, Fasshauer
776 D (2011) Primordial neurosecretory apparatus identified in the choanoflagellate Monosiga brevicollis.
777 *Proc Natl Acad Sci U S A* 108: 15264-15269

778 Caster AH, Kahn RA (2013) Recruitment of the Mint3 adaptor is necessary for export of the amyloid
779 precursor protein (APP) from the Golgi complex. *J Biol Chem* 288: 28567-28580

780 Chaufty J, Sullivan SE, Ho A (2012) Intracellular amyloid precursor protein sorting and amyloid-beta
781 secretion are regulated by Src-mediated phosphorylation of Mint2. *J Neurosci* 32: 9613-9625

782 Christie MP, Whitten AE, King GJ, Hu SH, Jarrott RJ, Chen KE, Duff AP, Callow P, Collins BM,
783 James DE *et al* (2012) Low-resolution solution structures of Munc18:Syntaxin protein complexes
784 indicate an open binding mode driven by the Syntaxin N-peptide. *Proc Natl Acad Sci U S A* 109:
785 9816-9821

786 Corpet F, Gouzy J, Kahn D (1999) Browsing protein families via the 'Rich Family Description' format.
787 *Bioinformatics* 15: 1020-1027

788 Dean C, Dresbach T (2006) Neuroligins and neurexins: linking cell adhesion, synapse formation and
789 cognitive function. *Trends Neurosci* 29: 21-29

790 Diella F, Haslam N, Chica C, Budd A, Michael S, Brown NP, Trave G, Gibson TJ (2008)
791 Understanding eukaryotic linear motifs and their role in cell signaling and regulation. *Front Biosci* 13:
792 6580-6603

793 Dunning CJ, Black HL, Andrews KL, Davenport EC, Conboy M, Chawla S, Dowle AA, Ashford D,
794 Thomas JR, Evans GJ (2016) Multisite tyrosine phosphorylation of the N-terminus of Mint1/X11alpha
795 by Src kinase regulates the trafficking of amyloid precursor protein. *J Neurochem* 137: 518-527

796 Evans R, O'Neill M, Pritzel A, Antropova N, Senior A, Green T, Žídek A, Bates R, Blackwell S, Yim
797 J *et al* (2022) Protein complex prediction with AlphaFold-Multimer. *bioRxiv*: 2021.2010.2004.463034

798 Evstratova A, Chamberland S, Faundez V, Toth K (2014) Vesicles derived via AP-3-dependent
799 recycling contribute to asynchronous release and influence information transfer. *Nat Commun* 5:
800 5530

801 Fasano G, Muto V, Radio FC, Venditti M, Mosaddeghzadeh N, Coppola S, Paradisi G, Zara E, Bazgir
802 F, Ziegler A *et al* (2022) Dominant ARF3 variants disrupt Golgi integrity and cause a
803 neurodevelopmental disorder recapitulated in zebrafish. *Nat Commun* 13: 6841

804 Gao M, Nakajima An D, Parks JM, Skolnick J (2022a) AF2Complex predicts direct physical
805 interactions in multimeric proteins with deep learning. *Nat Commun* 13: 1744

806 Gao M, Nakajima An D, Skolnick J (2022b) Deep learning-driven insights into super protein
807 complexes for outer membrane protein biogenesis in bacteria. *Elife* 11

808 Gotthardt M, Trommsdorff M, Nevitt MF, Shelton J, Richardson JA, Stockinger W, Nimpf J, Herz J
809 (2000) Interactions of the low density lipoprotein receptor gene family with cytosolic adaptor and
810 scaffold proteins suggest diverse biological functions in cellular communication and signal
811 transduction. *J Biol Chem* 275: 25616-25624

812 Graham ME, Prescott GR, Johnson JR, Jones M, Walmesley A, Haynes LP, Morgan A, Burgoyne
813 RD, Barclay JW (2011) Structure-function study of mammalian Munc18-1 and C. elegans UNC-18
814 implicates domain 3b in the regulation of exocytosis. *PLoS One* 6: e17999

Gross GG, Lone GM, Leung LK, Hartenstein V, Guo M (2013) X11/Mint genes control polarized localization of axonal membrane proteins in vivo. *J Neurosci* 33: 8575-8586

Han GA, Bin NR, Kang SY, Han L, Sugita S (2013) Domain 3a of Munc18-1 plays a crucial role at the priming stage of exocytosis. *J Cell Sci* 126: 2361-2371

Han GA, Park S, Bin NR, Jung CH, Kim B, Chandrasegaram P, Matsuda M, Riadi I, Han L, Sugita S (2014) A pivotal role for pro-335 in balancing the dual functions of Munc18-1 domain-3a in regulated exocytosis. *J Biol Chem* 289: 33617-33628

Hayashi S, Uehara DT, Tanimoto K, Mizuno S, Chinen Y, Fukumura S, Takanashi JI, Osaka H, Okamoto N, Inazawa J (2017) Comprehensive investigation of CASK mutations and other genetic etiologies in 41 patients with intellectual disability and microcephaly with pontine and cerebellar hypoplasia (MICPCH). *PLoS One* 12: e0181791

He X, Cooley K, Chung CH, Dashti N, Tang J (2007) Apolipoprotein receptor 2 and X11 alpha/beta mediate apolipoprotein E-induced endocytosis of amyloid-beta precursor protein and beta-secretase, leading to amyloid-beta production. *J Neurosci* 27: 4052-4060

Hill K, Li Y, Bennett M, McKay M, Zhu X, Shern J, Torre E, Lah JJ, Levey AI, Kahn RA (2003) Munc18 interacting proteins: ADP-ribosylation factor-dependent coat proteins that regulate the traffic of beta-Alzheimer's precursor protein. *J Biol Chem* 278: 36032-36040

Ho A, Liu X, Sudhof TC (2008) Deletion of Mint proteins decreases amyloid production in transgenic mouse models of Alzheimer's disease. *J Neurosci* 28: 14392-14400

Ho A, Morishita W, Hammer RE, Malenka RC, Sudhof TC (2003) A role for Mints in transmitter release: Mint 1 knockout mice exhibit impaired GABAergic synaptic transmission. *Proc Natl Acad Sci U S A* 100: 1409-1414

Ho CS, Marinescu V, Steinhilb ML, Gaut JR, Turner RS, Stuenkel EL (2002a) Synergistic Effects of Munc18a and X11 Proteins on Amyloid Precursor Protein Metabolism. *Journal of Biological Chemistry* 277: 27021-27028

Ho CS, Marinescu V, Steinhilb ML, Gaut JR, Turner RS, Stuenkel EL (2002b) Synergistic effects of Munc18a and X11 proteins on amyloid precursor protein metabolism. *J Biol Chem* 277: 27021-27028

Holehouse AS, Ahad J, Das RK, Pappu RV (2015) CIDER: Classification of Intrinsically Disordered Ensemble Regions. *Biophys J* 108: 228a.

Hornak V, Abel R, Okur A, Strockbine B, Roitberg A, Simmerling C (2006) Comparison of multiple Amber force fields and development of improved protein backbone parameters. *Proteins* 65: 712-725

Hornbeck PV, Zhang B, Murray B, Kornhauser JM, Latham V, Skrzypek E (2015) PhosphoSitePlus, 2014: mutations, PTMs and recalibrations. *Nucleic Acids Res* 43: D512-520

Hsueh YP (2009) Calcium/calmodulin-dependent serine protein kinase and mental retardation. *Ann Neurol* 66: 438-443

Hu SH, Christie MP, Saez NJ, Latham CF, Jarrott R, Lua LH, Collins BM, Martin JL (2011) Possible roles for Munc18-1 domain 3a and Syntaxin1 N-peptide and C-terminal anchor in SNARE complex formation. *Proc Natl Acad Sci U S A* 108: 1040-1045

Humphreys IR, Pei J, Baek M, Krishnakumar A, Anishchenko I, Ovchinnikov S, Zhang J, Ness TJ, Banjade S, Bagde SR *et al* (2021) Computed structures of core eukaryotic protein complexes. *Science* 374: eabm4805

857 Hung AY, Sheng M (2002) PDZ domains: structural modules for protein complex assembly. *J Biol*
858 *Chem* 277: 5699-5702

859 Huttlin EL, Bruckner RJ, Navarrete-Perea J, Cannon JR, Baltier K, Gebreab F, Gygi MP, Thornock
860 A, Zarraga G, Tam S *et al* (2021) Dual proteome-scale networks reveal cell-specific remodeling of
861 the human interactome. *Cell* 184: 3022-3040 e3028

862 Jones KA, Eng AG, Raval P, Srivastava DP, Penzes P (2014) Scaffold protein X11alpha interacts
863 with kalirin-7 in dendrites and recruits it to Golgi outposts. *J Biol Chem* 289: 35517-35529

864 Jumper J, Evans R, Pritzel A, Green T, Figurnov M, Ronneberger O, Tunyasuvunakool K, Bates R,
865 Zidek A, Potapenko A *et al* (2021) Highly accurate protein structure prediction with AlphaFold. *Nature*
866 596: 583-589

867 Kasula R, Blum A, Salla-Martret, Chai Ma, Jin Y, Jiang A, Wallis TP, Gormal RS, Brouillet JZ,
868 Padmanabhan P *et al* (2019) VAMP2 Binding to Munc18-1 Domain 3a Controls the Nanoscale
869 Reorganization of the Plasma Membrane and Vesicle Interface During Vesicular Priming. *Cell Press*
870 *Sneak Peak (Preprint)*

871 Kasula R, Chai YJ, Bademosi AT, Harper CB, Gormal RS, Morrow IC, Hosy E, Collins BM, Choquet
872 D, Papadopulos A *et al* (2016) The Munc18-1 domain 3a hinge-loop controls syntaxin-1A
873 nanodomain assembly and engagement with the SNARE complex during secretory vesicle priming.
874 *J Cell Biol* 214: 847-858

875 Kawabe H, Nakanishi H, Asada M, Fukuhara A, Morimoto K, Takeuchi M, Takai Y (2001) Pilt, a
876 novel peripheral membrane protein at tight junctions in epithelial cells. *J Biol Chem* 276: 48350-
877 48355

878 Ko J, Lee J (2021) Can AlphaFold2 predict protein-peptide complex structures accurately? *bioRxiv*:
879 2021.2007.2027.453972

880 Kondo M, Shiono M, Itoh G, Takei N, Matsushima T, Maeda M, Taru H, Hata S, Yamamoto T, Saito
881 Y *et al* (2010) Increased amyloidogenic processing of transgenic human APP in X11-like deficient
882 mouse brain. *Mol Neurodegener* 5: 35

883 Kondo Y, Hanai A, Nakai W, Katoh Y, Nakayama K, Shin HW (2012) ARF1 and ARF3 are required
884 for the integrity of recycling endosomes and the recycling pathway. *Cell Struct Funct* 37: 141-154

885 Kubala MH, Kovtun O, Alexandrov K, Collins BM (2010) Structural and thermodynamic analysis of
886 the GFP:GFP-nanobody complex. *Protein Sci* 19: 2389-2401

887 LaConte LEW, Chavan V, DeLuca S, Rubin K, Malc J, Berry S, Gail Summers C, Mukherjee K (2019)
888 An N-terminal heterozygous missense CASK mutation is associated with microcephaly and bilateral
889 retinal dystrophy plus optic nerve atrophy. *Am J Med Genet A* 179: 94-103

890 Lanoue V, Chai YJ, Brouillet JZ, Weckhuysen S, Palmer EE, Collins BM, Meunier FA (2019) STXBP1
891 encephalopathy: Connecting neurodevelopmental disorders with alpha-synucleinopathies?
892 *Neurology* 93: 114-123

893 Lee DS, Tomita S, Kirino Y, Suzuki T (2000) Regulation of X11L-dependent amyloid precursor
894 protein metabolism by XB51, a novel X11L-binding protein. *J Biol Chem* 275: 23134-23138

895 Lee HY, Park JB, Jang IH, Chae YC, Kim JH, Kim IS, Suh PG, Ryu SH (2004) Munc-18-1 inhibits
896 phospholipase D activity by direct interaction in an epidermal growth factor-reversible manner. *J Biol*
897 *Chem* 279: 16339-16348

898 Lee JH, Lau KF, Perkinton MS, Standen CL, Shemilt SJ, Mercken L, Cooper JD, McLoughlin DM,
899 Miller CC (2003) The neuronal adaptor protein X11alpha reduces Abeta levels in the brains of
900 Alzheimer's APPswe Tg2576 transgenic mice. *J Biol Chem* 278: 47025-47029

901 Lee Y, Kim BS, Choi S, Lee EY, Park S, Hwang J, Kwon Y, Hyun J, Lee C, Kim JF *et al* (2019)
902 Makes caterpillars floppy-like effector-containing MARTX toxins require host ADP-ribosylation factor
903 (ARF) proteins for systemic pathogenicity. *Proc Natl Acad Sci U S A* 116: 18031-18040

904 Leonoudakis D, Conti LR, Radeke CM, McGuire LM, Vandenberg CA (2004) A multiprotein
905 trafficking complex composed of SAP97, CASK, Veli, and Mint1 is associated with inward rectifier
906 Kir2 potassium channels. *J Biol Chem* 279: 19051-19063

907 Li P, Merrill SA, Jorgensen EM, Shen K (2016) Two Clathrin Adaptor Protein Complexes Instruct
908 Axon-Dendrite Polarity. *Neuron* 90: 564-580

909 Li W, Xing Y, Wang Y, Xu T, Song E, Feng W (2023) A non-canonical target-binding site in Munc18-
910 1 domain 3b for assembling the Mint1-Munc18-1-syntaxin-1 complex. *Structure* 31: 68-77 e65

911 Lin AY, Henry S, Reissner C, Neupert C, Kenny C, Missler M, Beffert U, Ho A (2019) A rare autism-
912 associated MINT2/APBA2 mutation disrupts neurexin trafficking and synaptic function. *Sci Rep* 9:
913 6024

914 Long JF, Feng W, Wang R, Chan LN, Ip FC, Xia J, Ip NY, Zhang M (2005) Autoinhibition of X11/Mint
915 scaffold proteins revealed by the closed conformation of the PDZ tandem. *Nat Struct Mol Biol* 12:
916 722-728

917 M. Okamoto TCSd (1997) Mints, Munc18-interacting proteins in synaptic vesicle exocytosis. *J Biol*
918 *Chem* 272

919 Mardones GA, Burgos PV, Lin Y, Kloer DP, Magadan JG, Hurley JH, Bonifacino JS (2013) Structural
920 basis for the recognition of tyrosine-based sorting signals by the mu3A subunit of the AP-3 adaptor
921 complex. *J Biol Chem* 288: 9563-9571

922 Martin S, Tomatis VM, Papadopulos A, Christie MP, Malintan NT, Gormal RS, Sugita S, Martin JL,
923 Collins BM, Meunier FA (2013) The Munc18-1 domain 3a loop is essential for neuroexocytosis but
924 not for syntaxin-1A transport to the plasma membrane. *J Cell Sci* 126: 2353-2360

925 Matos MF, Xu Y, Dulubova I, Otwinowski Z, Richardson JM, Tomchick DR, Rizo J, Ho A (2012)
926 Autoinhibition of Mint1 adaptor protein regulates amyloid precursor protein binding and processing.
927 *Proc Natl Acad Sci U S A* 109: 3802-3807

928 Maximov A, Sudhof TC, Bezprozvanny I (1999) Association of neuronal calcium channels with
929 modular adaptor proteins. *J Biol Chem* 274: 24453-24456

930 McLoughlin DM, Standen CL, Lau KF, Ackerley S, Bartnikas TP, Gitlin JD, Miller CC (2001) The
931 neuronal adaptor protein X11alpha interacts with the copper chaperone for SOD1 and regulates
932 SOD1 activity. *J Biol Chem* 276: 9303-9307

933 Miesenbock G, De Angelis DA, Rothman JE (1998) Visualizing secretion and synaptic transmission
934 with pH-sensitive green fluorescent proteins. *Nature* 394: 192-195

935 Minami SS, Sung YM, Dumanis SB, Chi SH, Burns MP, Ann EJ, Suzuki T, Turner RS, Park HS, Pak
936 DT *et al* (2010) The cytoplasmic adaptor protein X11alpha and extracellular matrix protein Reelin
937 regulate ApoE receptor 2 trafficking and cell movement. *FASEB J* 24: 58-69

938 Mirdita M, Schutze K, Moriwaki Y, Heo L, Ovchinnikov S, Steinegger M (2022) ColabFold: making
939 protein folding accessible to all. *Nat Methods* 19: 679-682

940 Mirdita M, Steinegger M, Soding J (2019) MMseqs2 desktop and local web server app for fast,
941 interactive sequence searches. *Bioinformatics* 35: 2856-2858

942 Motodate R, Saito H, Sobu Y, Hata S, Saito Y, Nakaya T, Suzuki T (2019) X11 and X11-like proteins
943 regulate the level of extrasynaptic glutamate receptors. *J Neurochem* 148: 480-498

944 Motodate R, Saito Y, Hata S, Suzuki T (2016) Expression and localization of X11 family proteins in
945 neurons. *Brain Res* 1646: 227-234

946 Nakai W, Kondo Y, Saitoh A, Naito T, Nakayama K, Shin HW (2013) ARF1 and ARF4 regulate
947 recycling endosomal morphology and retrograde transport from endosomes to the Golgi apparatus.
948 *Mol Biol Cell* 24: 2570-2581

949 Newell-Litwa K, Chintala S, Jenkins S, Pare JF, McGaha L, Smith Y, Faundez V (2010) Hermansky-
950 Pudlak protein complexes, AP-3 and BLOC-1, differentially regulate presynaptic composition in the
951 striatum and hippocampus. *J Neurosci* 30: 820-831

952 Nourry C, Grant SG, Borg JP (2003) PDZ domain proteins: plug and play! *Sci STKE* 2003: RE7

953 Okamoto M, Sudhof TC (1997) Mints, Munc18-interacting proteins in synaptic vesicle exocytosis. *J*
954 *Biol Chem* 272: 31459-31464

955 Okamoto M, Sudhof TC (1998) Mint 3: a ubiquitous mint isoform that does not bind to munc18-1 or
956 -2. *Eur J Cell Biol* 77: 161-165

957 Oughtred R, Rust J, Chang C, Breitkreutz BJ, Stark C, Willems A, Boucher L, Leung G, Kolas N,
958 Zhang F *et al* (2021) The BioGRID database: A comprehensive biomedical resource of curated
959 protein, genetic, and chemical interactions. *Protein Sci* 30: 187-200

960 Papadopulos A, Martin S, Tomatis VM, Gormal RS, Meunier FA (2013) Secretagogue stimulation of
961 neurosecretory cells elicits filopodial extensions uncovering new functional release sites. *J Neurosci*
962 33: 19143-19153

963 Park JH, Jung MS, Kim YS, Song WJ, Chung SH (2012) Phosphorylation of Munc18-1 by Dyrk1A
964 regulates its interaction with Syntaxin 1 and X11alpha. *J Neurochem* 122: 1081-1091

965 Peleg Y, Vincentelli R, Collins BM, Chen KE, Livingstone EK, Weeratunga S, Leneva N, Guo Q,
966 Remans K, Perez K *et al* (2021) Community-Wide Experimental Evaluation of the PROSS Stability-
967 Design Method. *J Mol Biol* 433: 166964

968 Penzes P, Johnson, R.C., Sattler, R., Zhang, X., Huganir, R.L., Kambampati, V., Mains, R.E., Eipper,
969 B.A., (2001) The neuronal Rho-GEF Kalirin-7 interacts with PDZ domain-containing proteins and
970 regulates dendritic morphogenesis. *Neuron* 29: 229–242

971 Peycheva V, Kamenarova K, Ivanova N, Stamatov D, Avdjieva-Tzavella D, Alexandrova I,
972 Zhelyazkova S, Pacheva I, Dimova P, Ivanov I *et al* (2018) Chromosomal microarray analysis of
973 Bulgarian patients with epilepsy and intellectual disability. *Gene* 667: 45-55

974 Piluso G, D'Amico F, Saccone V, Bismuto E, Rotundo IL, Di Domenico M, Aurino S, Schwartz CE,
975 Neri G, Nigro V (2009) A missense mutation in CASK causes FG syndrome in an Italian family. *Am*
976 *J Hum Genet* 84: 162-177

977 Poetz F, Corbo J, Levdansky Y, Spiegelhalter A, Lindner D, Magg V, Lebedeva S, Schweiggert J,
978 Schott J, Valkov E *et al* (2021) RNF219 attenuates global mRNA decay through inhibition of CCR4-
979 NOT complex-mediated deadenylation. *Nature Communications* 12: 7175

980 Robert X, Gouet P (2014) Deciphering key features in protein structures with the new ENDscript
981 server. *Nucleic Acids Res* 42: W320-324

Rogelj B, Mitchell JC, Miller CC, McLoughlin DM (2006) The X11/Mint family of adaptor proteins. *Brain Res Rev* 52: 305-315

Saito Y, Akiyama M, Araki Y, Sumioka A, Shiono M, Taru H, Nakaya T, Yamamoto T, Suzuki T (2011) Intracellular trafficking of the amyloid beta-protein precursor (APP) regulated by novel function of X11-like. *PLoS One* 6: e22108

Sakamoto M, Sasaki K, Sugie A, Nitta Y, Kimura T, Gursoy S, Cinleti T, Iai M, Sengoku T, Ogata K *et al* (2021) De novo ARF3 variants cause neurodevelopmental disorder with brain abnormality. *Hum Mol Genet* 31: 69-81

Sakuma M, Tanaka E, Taru H, Tomita S, Gandy S, Nairn AC, Nakaya T, Yamamoto T, Suzuki T (2009) Phosphorylation of the amino-terminal region of X11L regulates its interaction with APP. *J Neurochem* 109: 465-475

Saluja I, Paulson H, Gupta A, Turner RS (2009) X11alpha haploinsufficiency enhances Abeta amyloid deposition in Alzheimer's disease transgenic mice. *Neurobiol Dis* 36: 162-168

Sanger A, Hirst J, Davies AK, Robinson MS (2019) Adaptor protein complexes and disease at a glance. *J Cell Sci* 132

Sano Y, Syuzo-Takabatake A, Nakaya T, Saito Y, Tomita S, Itohara S, Suzuki T (2006) Enhanced amyloidogenic metabolism of the amyloid beta-protein precursor in the X11L-deficient mouse brain. *J Biol Chem* 281: 37853-37860

Schneider CA, Rasband WS, Eliceiri KW (2012) NIH Image to ImageJ: 25 years of image analysis. *Nat Methods* 9: 671-675

Schubert E, Sander J, Ester M, Kriegel HP, Xu X (2017) DBSCAN Revisited, Revisited: Why and How You Should (Still) Use DBSCAN. *ACM Trans Database Syst* 42: Article 19

Seong E, Wainer BH, Hughes ED, Saunders TL, Burmeister M, Faundez V (2005) Genetic analysis of the neuronal and ubiquitous AP-3 adaptor complexes reveals divergent functions in brain. *Mol Biol Cell* 16: 128-140

Shetty A, Sytnyk V, Leshchyns'ka I, Puchkov D, Haucke V, Schachner M (2013) The neural cell adhesion molecule promotes maturation of the presynaptic endocytotic machinery by switching synaptic vesicle recycling from adaptor protein 3 (AP-3)- to AP-2-dependent mechanisms. *J Neurosci* 33: 16828-16845

Sifri C, Hoeg L, Durocher D, Setiaputra D (2023) An AlphaFold2 map of the 53BP1 pathway identifies a direct SHLD3-RIF1 interaction critical for DNA repair activity. *bioRxiv*: 2023.2001.2012.523815

Simonetti B, Guo Q, Gimenez-Andres M, Chen K-E, Moody ERR, Evans AJ, Danson CM, Williams TA, Collins BM, Cullen PJ (2021) Mechanistic basis for SNX27-Retromer coupling to ESCPE-1 in promoting endosomal cargo recycling. *bioRxiv*: 2021.2008.2028.457928

Stafford RL, Ear J, Knight MJ, Bowie JU (2011) The molecular basis of the Caskin1 and Mint1 interaction with CASK. *J Mol Biol* 412: 3-13

Stepien KP, Xu J, Zhang X, Bai XC, Rizo J (2022) SNARE assembly enlightened by cryo-EM structures of a synaptobrevin-Munc18-1-syntaxin-1 complex. *Sci Adv* 8: eabo5272

Sullivan SE, Dillon GM, Sullivan JM, Ho A (2014) Mint proteins are required for synaptic activity-dependent amyloid precursor protein (APP) trafficking and amyloid beta generation. *J Biol Chem* 289: 15374-15383

Tabuchi K, Biederer T, Butz S, Sudhof TC (2002) CASK participates in alternative tripartite complexes in which Mint 1 competes for binding with caskin 1, a novel CASK-binding protein. *J Neurosci* 22: 4264-4273

Tamaki H, Sanda M, Katsumata O, Hara Y, Fukaya M, Sakagami H (2012) Pilt is a coiled-coil domain-containing protein that localizes at the trans-Golgi complex and regulates its structure. *FEBS Lett* 586: 3064-3070

Tomita S, Fujita T, Kirino Y, Suzuki T (2000) PDZ domain-dependent suppression of NF-kappaB/p65-induced Abeta42 production by a neuron-specific X11-like protein. *J Biol Chem* 275: 13056-13060

Tomita S, Ozaki T, Taru H, Oguchi S, Takeda S, Yagi Y, Sakiyama S, Kirino Y, Suzuki T (1999) Interaction of a neuron-specific protein containing PDZ domains with Alzheimer's amyloid precursor protein. *J Biol Chem* 274: 2243-2254

Tsaban T, Varga J, Avraham O, Ben-Aharon Z, Khramushin A, Schueler-Furman O (2021) Harnessing protein folding neural networks for peptide-protein docking. *bioRxiv*: 2021.2008.2001.454656

Verhage M, Sorensen JB (2020) SNAREopathies: Diversity in Mechanisms and Symptoms. *Neuron* 107: 22-37

Voglmaier SM, Kam K, Yang H, Fortin DL, Hua Z, Nicoll RA, Edwards RH (2006) Distinct endocytic pathways control the rate and extent of synaptic vesicle protein recycling. *Neuron* 51: 71-84

Wu X, Cai Q, Chen Y, Zhu S, Mi J, Wang J, Zhang M (2020) Structural Basis for the High-Affinity Interaction between CASK and Mint1. *Structure* 28: 664-673 e663

Xie X, Yan X, Wang Z, Zhou H, Diao W, Zhou W, Long J, Shen Y (2013) Open-closed motion of Mint2 regulates APP metabolism. *J Mol Cell Biol* 5: 48-56

Ye F, Zeng M, Zhang M (2018) Mechanisms of MAGUK-mediated cellular junctional complex organization. *Curr Opin Struct Biol* 48: 6-15

Yu D, Chojnowski G, Rosenthal M, Kosinski J (2023) AlphaPulldown-a python package for protein-protein interaction screens using AlphaFold-Multimer. *Bioinformatics* 39

Zhang Y, Wang YG, Zhang Q, Liu XJ, Liu X, Jiao L, Zhu W, Zhang ZH, Zhao XL, He C (2009) Interaction of Mint2 with TrkA is involved in regulation of nerve growth factor-induced neurite outgrowth. *J Biol Chem* 284: 12469-12479

Zhang Z, Lee CH, Mandiyan V, Borg JP, Margolis B, Schlessinger J, Kuriyan J (1997) Sequence-specific recognition of the internalization motif of the Alzheimer's amyloid precursor protein by the X11 PTB domain. *EMBO J* 16: 6141-6150

Zhang Z, Li W, Yang G, Lu X, Qi X, Wang S, Cao C, Zhang P, Ren J, Zhao J *et al* (2020) CASK modulates the assembly and function of the Mint1/Munc18-1 complex to regulate insulin secretion. *Cell Discov* 6: 92

Figure legends

Figure 1. The Mint1 MID interacts directly with Munc18-1 but not Munc18-3

(A) Schematic diagram of the human Mint proteins. (AHM, acidic α-heilcal motif; MID, Munc18-1-interacting domain; CID, CASK interacting domain; PTB, phosphotyrosine binding domain; PDZ1 and PDZ2, Psd95/Dlg/ZO1 domains). **(B)** Pulldowns with GST-Mint1 MID show a direct interaction with purified Munc18-1 but not Munc18-3. Image shows Coomassie Blue stained gel. **(C)** Pulldowns with GST-tagged Mint1 truncated sequences identify residues 261-282 as sufficient and required for Munc18-1 binding. Image shows Coomassie Blue stained gel.

Figure 2. A conserved sequence in Mint1 and Mint2 binds Munc18-1 and is not influenced by phosphorylation

(A) ITC of synthetic Mint1$^{261-282}$ peptide binding to purified Munc18-1. The top shows raw ITC data, and the bottom shows integrated and normalised data fit to a 1:1 binding model. **(B)** Sequences of peptides tested for Munc18-1 binding by ITC. The minimal and highly conserved sequence required for Munc18-1 binding is shaded. Mutated peptide residues are highlighted in blue. **(C)** Endogenous Munc18-1 is bound to GFP-tagged Mint1 but not the mutant GFP-Mint1$^{D269A/I270A}$. GFP-tagged Mint1 proteins were transiently transfected into PC12 cells, immunoprecipitated with GFP-nanobody coupled beads, and the bound proteins probed by Western blot with anti-Munc18-1.

Figure 3. Modelling of Munc18-1 in complex with the Mint1 AHM sequence.

(A) AlphaFold2 prediction of the complex between Munc18-1 and Mint1 AHM. The three top ranked models are overlaid and shown in backbone ribbon representation. The AHM is consistently modelled in an α-helical structure associated with the Munc18-1 domain3b (highlighted in blue). On the right the predicted alignment error (PAE) is plotted for each model. Signals in the off-diagonal regions indicate strong structural correlations between residues in the peptide with the Munc18-1 protein. **Fig. S4** shows predictions of the full-length Munc18-1 and Mint1 complex as well as models of other Munc and Mint homologues and orthologues. (**B**) The top-ranked complex of Munc18-1 and the Mint1 AHM is shown in cartoon representation, with Munc18-1 domains highlighted. (**C**) As in (**B**) but the surface of Munc18-1 is shown coloured for sequence conservation as calculated by Consurf (Ashkenazy *et al.*, 2016). (**D**) Opposite views showing details of the Mint1 AHM bound to the Munc18-1 domain3b. (**E**) ITC of synthetic Mint1$^{261-282}$ peptide binding to purified Munc18-1 and structure-based mutants. The top shows raw ITC data, and the bottom shows integrated and normalised data fit to a 1:1 binding model. Mutated residues are highlighted in panel (**D**). (**F**) Cumulative release events over time for each data group was analysed and the number of release events at each 10 sec interval from 0-290 sec was determined, plotted as MEAN±SEM. (**G**) Total evoked release events following stimulation were measured per μm^2. Non-parametric Mann Whitney U test, $p < 0.05$, *, $p < 0.01$. N = 15 cells (WT) and 17 (R388A) from independent experiments.

1100 **Figure 4. Comparison of the predicted Munc18-1/Mint1 complex with experimental structures.**
1101 (**A**) Overlay of the Munc18-1 complex with Mint1 AHM predicted by AlphaFold2 and the recent crystal
1102 structure of the Munc18-1/Sx1a/Mint1 complex (Li *et al.*, 2023). The inset shows details of the
1103 binding site modelled by AlphaFold2 and observed in the crystal structure. The two structures are
1104 identical in all key respects. (**B**) Overlay of the Munc18-1 complex with Mint1 AHM predicted by
1105 AlphaFold2 and the cryoEM structure of the Munc18-1/Sx1a/VAMP2 complex (Stepien *et al.*, 2022).
1106 The Mint1 AHM is expected to bind Munc18-1 independently of the Sxa1 t-SNARE and VAMP2 v-
1107 SNARE proteins.
1108
1109 **Figure 5. Mint1 and Sx1a show allosteric effects on binding to Munc18-1**
1110 **(A)** Pulldowns with GST-Mint1 MID show that Munc18-1 domain3a hinge loop is important for binding.
1111 As Mint1 does not contact domain3a this suggests an allosteric effect on the domain3b binding site.
1112 Image shows Coomassie stained gel. **(B)** ITC of synthetic Mint1$^{261\text{-}282}$ peptide binding to purified
1113 Munc18-1 (red) and Munc18-1$^{\Delta 317\text{-}333}$ (black) confirm the requirement of domain3a for Mint1
1114 interaction. **(C)** Pulldowns with GST-Mint1 MID show that Mint1 can bind Munc18-1 both alone and
1115 in the presence of Sx1a. Image shows Coomassie stained gel. **(D)** Although Mint1 and Sx1a can
1116 bind Munc18 simultaneously, ITC of Mint1 Mint1$^{261\text{-}282}$ AHM peptide binding to Munc18-1 in the
1117 absence (red) and presence (black) of Sx1a shows a reduction in binding affinity and enthalpy. **(E)**
1118 ITC of Sx1a binding to Munc18-1 in the absence (black) and presence (red) of synthetic Mint1$^{261\text{-}282}$
1119 peptide. Together this shows there is a subtle allosteric inhibition of Sxa1 binding to Munc18-1 in the
1120 presence of Mint1. **(F)** ITC of Sx1a binding to Munc18-1$^{\Delta 317\text{-}333}$ in the absence (black) and presence
1121 (red) of synthetic Mint1$^{261\text{-}282}$ peptide.
1122
1123 **Figure 6. Interactions of the Mint PTB domains with canonical NPxY-containing peptide**
1124 **motifs predicted by AlphaFold2**
1125 Overlay of the top-ranked AlphaFold2 predicted structures of the Mint1 PTB domain (blue) in
1126 complex with various NPxY-related peptide motifs (green) shown in backbone ribbon representation.
1127 These sequences are predicted to bind the canonical binding groove of the PTB domain (with similar
1128 interactions predicted for Mint2 (not shown)). The right panel shows details of the different
1129 sequences derived from various Mint-interacting transmembrane proteins.
1130
1131 **Figure 7. Interactions of the Mint PTB domains with a non-canonical peptide motif from TJAP1**
1132 **predicted by AlphaFold2**
1133 (**A**) Overlay of the top-ranked AlphaFold2 predicted structures of the Mint1 and Mint2 PTB domains
1134 (blue) in complex with the APP NPxY motif (green) and the N-terminal peptide of TJAP1 (brown)
1135 shown in backbone ribbon representation. (**B**) The top-ranked complex of Mint1 PTB domain bound
1136 to APP and TJAP1 is shown in cartoon representation. The lower panel shows the surface of Mint1
1137 coloured for sequence conservation as calculated by Consurf (Ashkenazy *et al.*, 2016). (**C**) Details

of the Mint1 PTB domain interaction with the TJAP1 peptide. (**D**) ITC of Mint1 PTB binding to the peptide motif from APP in the presence and absence of a peptide from TJAP1. (**E**) ITC of Mint1 PTB binding to the peptide motif from TJAP1 in the presence and absence of a peptide from APP. The top shows raw ITC data, and the bottom shows integrated and normalised data fit to a 1:1 binding model.

Figure 8. Interactions of the Mint N-terminus and PDZ domains with novel binders predicted by AlphaFold2

(**A**) Overlay of the top-ranked AlphaFold2 predicted structures of the Mint1 and Mint2 tandem PDZ domains (blue) in complex with ARF3 and ARF4 (green) shown in backbone ribbon representation. The middle panel shows the Mint1 complex with ARF3 in ribbon representation, with the position of GTP and Mg^{2+} based on the previous crystal structure of active ARF3-GTP (Lee *et al.*, 2019). The right panel shows the same image but with Mint1 surface coloured for sequence conservation as calculated by Consurf (Ashkenazy *et al.*, 2016). (**B**) Overlay of the top-ranked AlphaFold2 predicted structures of the Mint1 and Mint2 tandem PDZ domains (blue) in complex with the C-terminal PDZbm of NRX1 (green) shown in backbone ribbon representation. The middle panel shows the Mint1 complex with ARF3 in ribbon representation. The right panel inset shows the details of the NRX1 interaction with Mint1 PDZ2 domain. (**C**) Overlay of the top three ranked AlphaFold2 predicted structures of the Mint1 YxxΦ motif (blue) in complex with the C-terminal MHD of the AP3 μ3A subunit (green) shown in backbone ribbon representation. The middle panel shows the Mint1 complex with μ3A in ribbon representation. The right panel inset shows the details of the Mint1 YxxΦ motif interaction with μ3A.

Figure 9. Mint1 structural model and interactions.

(**A**) Structural model of Mint1 derived from AlphaFold2 (Ammann *et al.*, 2016). (**B**) Schematic summary of Mint1-mediated interactions, and speculative model suggesting that at the cell surface Mint1 may act to reduce the affinity of Munc18-1 for the auto-inhibited Sx1a, thus enhancing the ability of Sx1a to associate with VAMP2 and SNAP25 to form the trans-SNARE assembly required for vesicle fusion. The C-terminal domains of Mint1 in contrast are associated with other proteins containing NPxY and PDZbm sequences and ARF small GTPases that may enhance Mint1 membrane recruitment and modulate transmembrane protein trafficking.

1170 **Supplementary Information**

1171 **Figure S1. Sequence alignment of Mint proteins. (Related to Fig. 1)**

1172 (**A**) Sequence alignment Mint1 and Mint2. Alignment was performed with Multalin (Corpet *et al*, 1999)
1173 and rendered with ESPript3.0 (Robert & Gouet, 2014). Hs, *Homo sapiens*. Xt, *Xenopus tropicalis*.
1174 Dr, *Danio rerio*. Ce, *Caenorhabditis elegans*. Dv, *Drosophila virilis*.

1175

1176 **Figure S2. ITC experiments of Munc18-1 binding to various Mint peptides. (Related to Fig. 2)**

1177 Example ITC experiments are shown for each of the Mint peptides binding to Munc18-1 as described
1178 in **Fig. 2B** and Table 1. (**A**) Mint 1_1 (261-282) (**B**) Mint 1_1a (273-282) (**C**) Mint 1_1b (261-272) (**D**)
1179 Mint 1_1c (266-282) (**E**) Mint 1_4 (263-282) (**F**) Mint 1_5 (265-282) (**G**) Mint 1_6 (267-282) (**H**) Mint
1180 1_7 (261-280) (**I**) Mint 1_9 (261-276) (**J**) Mint 1_11 DI /AA (261-282 (**K**) Mint 1-12 DQ /AA (261-282)
1181 (**L**) Mint 1_13 IV/AA(261-282) (**M**) Mint 1_14 AE/AA(261-282) (**N**) Mint 1_2 (257-286) (**O**) Mint 1_3
1182 phosphomimetic (261-282) (**P**) Mint 2_2 phosphomimetic (219-242).

1183

1184 **Figure S3. Post-translational modifications and sequence charge distribution of human Mint1**
1185 **and Mint2. (Related to Fig. 2)**

1186 (**A**) Sites of phosphorylation and ubiquitination of human Mint1 and Mint2 experimentally observed
1187 and reported in PhosphoSitePlus (Hornbeck *et al.*, 2015). **(B)** Phosphorylation sites in the human
1188 Mint1 and Mint2 N-terminal regions documented in PhosphoSitePlus (Hornbeck *et al.*, 2015).
1189 Phosphomimetic mutations in regions adjacent to the Munc18-1 binding sequence do not influence
1190 affinity (**Fig. 2B; Table 1**). (**C**) Plot of the charge distribution versus the sequence of Mint1 and Mint2
1191 shows that the N-terminal disordered sequences have a high net-positive charge. Plots were made
1192 with CIDER (Holehouse *et al*, 2015).

1193

1194 **Figure S4. AlphaFold2 modelling of Munc18 interactions with Mint1. (Related to Fig. 3)**

1195 (**A**) Overlaid top three ranked models of human Mint1 bound to Munc18-1 from ColabFold shown in
1196 backbone ribbon representation. Mint1 is consistently modelled to bind Munc18-1 domain 3b via a
1197 short acidic α-helical motif (AHM) within its unstructured N-terminal domain (highlighted in blue). On
1198 the right hand side the predicted alignment error (PAE) is plotted for each model. Signals in the off-
1199 diagonal regions indicate strong structural correlations between residues in the peptide with the
1200 Munc18-1 protein. (**B**) Overlaid top three ranked models of the zebrafish Mint1 AHM sequence
1201 bound to Munc18-1 predicted with ColabFold. Similar to the human structures, the AHM is
1202 consistently modelled in an α-helical structure associated with the Munc18-1 domain3b (highlighted
1203 in blue). (**C**) Overlaid top three ranked models of the human Mint2 AHM sequence bound to Munc18-
1204 1 predicted with ColabFold. (**D**) Overlaid top three ranked models of the human Mint1 AHM
1205 sequence modelled with the non-binding Munc18-3 homologue. The AHM is modelled at several
1206 random positions (highlighted in blue). The PAE plots do not show evidence of significant interactions
1207 between the two proteins. (**E**) The top scoring model of the human Mint1 AHM and CID sequences

bound to Munc18-1 and CASK using ColabFold. The AHM region is predicted in an identical binding site on Munc18-1 to the isolated peptide sequence (highlighted in blue). The CID sequence is predicted to bind to CASK in almost essentially the same conformation as the two previous crystal structures (Wu *et al.*, 2020; Zhang *et al.*, 2020).

Figure S5. Analysis of cell footprint and fusion events in Munc18 DKO PC12 cells.
Representative fluorescent release event visualisation. The imaging dataset was divided into 10 sec (100 frame) intervals and the fluorescence averaged. Vesicle fusions at each interval were determined by Laplacian of Gaussian and used to create a 3D [x,y,t] array. DBSCAN was used to determine clusters of fluorescent areas/vesicles which persisted in the same area over time. A release event was defined as the end of each cluster.

Figure S6. AlphaFold2 modelling of Mint1 interactions with proteins identified in BioGRID. (Related to Fig. 5 and 6)
Proteins identified in BioGRID as putative interactors of Mint1 and showing reasonable binding in AlphaFold2 predictions. The left panels show the top three ranked structures overlaid in backbone ribbon representation. On the right hand side, the predicted alignment error (PAE) is plotted for each model. Signals in the off-diagonal regions indicate strong structural correlations between residues in the peptide with the Mint1 protein. These focused predictions were performed on specific Mint1 domains with the ligand regions initially identified in high-throughput predictions of the two full-length proteins.

Figure S7. AlphaFold2 modelling of Mint2 interactions with proteins identified in BioGRID. (Related to Fig. 5 and 6)
Proteins identified in BioGRID as putative interactors of Mint2 and showing reasonable binding in AlphaFold2 predictions. The left panels show the top three ranked structures overlaid in backbone ribbon representation. On the right hand side the predicted alignment error (PAE) is plotted for each model. Signals in the off-diagonal regions indicate strong structural correlations between residues in the peptide with the Mint2 protein. These focused predictions were performed on specific Mint2 domains with the ligand regions initially identified in high-throughput predictions of the two full-length proteins.

1239 **Table 1: Thermodynamic parameters of Munc18-1 binding to Mint1 by ITC.**

1240

Syringe Sample	Peptide residues	Peptide sequences	K_d (μM)	N	Δ*H* (kcal/mol)	-TΔ*S* (kcal/mol)	Δ*G* (kcal/mol)
Mint1_1	261-282	MDSYEQEEDIDQIVAEVKQSMS	12.8	0.8	-9.51	2.84	-6.67
Mint1_1a	273-282	IVAEVKQSMS	-	/	/	/	/
Mint1_1b	261-272	MDSYEQEEDIDQ	-	/	/	/	/
Mint1_1c	266-282	QEEDIDQIVAEVKQSMS	21.	1	-1.16	-5.21	-6.38
Mint1_4	263-282	SYEQEEDIDQIVAEVKQSMS	12.9	1.3	-2.3	-4.38	-6.70
Mint1_5	265-282	EQEEDIDQIVAEVKQSMS	5.6	1.3	-3.48	-3.69	-7.17
Mint1_6	267-282	EEDIDQIVAEVKQSMS	4.0	1.2	-1.29	-6.08	-7.37
Mint1_7	261-280	MDSYEQEEDIDQIVAEVKQS	19.1	1	-1.78	-4.67	-6.44
Mint1_8	261-278	MDSYEQEEDIDQIVAEVK	-	/	/	/	/
Mint1_9	261-276	MDSYEQEEDIDQIVAE	-	/	/	/	/
Mint1_10	261-282 E267A/E268A	MDSYEQAADIDQIVAEVKQSMS	-	/	/	/	/
Mint1_11	261-282 D269A/I270A	MDSYEQEEAADQIVAEVKQSMS	-	/	/	/	/
Mint1_12	261-282 D271A/Q272A	MDSYEQEEDIAAIVAEVKQSMS	-	/	/	/	/
Mint1_13	261-282 I273A/V274A	MDSYEQEEDIDQAAAEVKQSMS	-	/	/	/	/
Mint1_14	261-282 A275A/E276A	MDSYEQEEDIDQIVAAVKQSMS	216	1.0	-57.6	52.6	-5.00
Mint1_2	257-286	PYPRMDSYEQEEDIDQIVAEVKQSMSSQSL	26.0	**1.3**	-4.21	-3.41	-7.62
Mint1_3	257-286 phosphomimic	PYPRMDEEEQEEDIDQIVAEVKQEMEEQEL	14.0	1.1	-6.5	-0.103	-6.60
Mint2_2	219-242 phosphomimic	LEDQEEDIDQIVAEIKMELEMEEI	200	1	-17.2	12.2	-5.05

1241

1242

1243 **Table 2: Thermodynamic parameters of Munc18-1 binding to Sx1a and Mint1(261-**
1244 **282) by ITC.**
1245

Syringe sample	Cell Sample	K_d (μM)	N	Δ*H* (kcal/mol)	-TΔ*S* (kcal/mol)	Δ*G* (kcal/mol)	Fold increase in K_d
Sx1a	Munc18-1	0.07	1	-20.6	9.5	-11.1	1
Sx1a +Mint1	Munc18-1 +Mint1	0.27	1	-29.7	20.7	-9.0	35
Mint1	Munc18-1	8.7	1	-7.9	0.9	-7.0	1
Mint1	Munc18-1 +Sx1a	20.6	1	-8.9	2.5	-6.4	2
Sx1a	Munc18-1$^{\Delta 317-333}$	0.11	1	-18.6	9.1	-9.5	1
Sx1a +Mint1	Munc18-1$^{\Delta 317-333}$ +Mint1	0.09	1	-18.8	9.2	-9.6	1

1246
1247

1248 **Table 3: Thermodynamic parameters of Mint1 PTB domain binding to TJAP1 and**
1249 **APP peptides by ITC.**
1250

Syringe sample	Cell Sample	K_d (μM)	N	Δ*H* (kcal/mol)	-TΔ*S* (kcal/mol)	Δ*G* (kcal/mol)
TJAP1(9-22)	Mint1 PTB	37.3	1	-10.3	4.1	-6.4
TJAP1(9-22)	Mint1 PTB + APP(750-769)	29.4	1	-7.1	0.9	-6.2
APP(750-769)	Mint1 PTB	0.31	1	-15.6	6.7	-8.9
APP(750-769)	Mint1 PTB + TJAP1(9-22)	0.58	1	-11.8	3.3	-8.5

1251
1252

1253 **Resources Table.**

1254

REAGENT or RESOURCE	SOURCE or REFERENCE	IDENTIFIER
Bacterial Strains		
E. coli DH5α	Invitrogen	18265017
E. coli Rosetta™(DE3)	Merck Australia	70954
Cell Lines		
Pheochromocytoma cells (PC12)	ATCC	CRL-1721
Antibodies		
GFP polyclonal antibody	Thermo Fisher	A6455
BD Mouse Monoclonal anti-Munc18-1	BD Biosciences	610336
Goat anti mouse secondary antibody	Thermo Fisher	65-6120
Chemicals		
Benzamidine hydrochloride hydrate	Sigma Aldrich	B6506
Deoxyribonuclease I (DNase I)	Sigma Aldrich	DN25
Talon® resin	Clontech	635503
Glutathione Sepharose 4B	GE Healthcare	GEHE17-0756-0
Isopropyl β-D-1-thiogalactopyranoside	Bioline	BIO-37036
LipofectamineTM LTX with PLUS ReagentTM	ThermoFisher	15338-100
Poly-D-Lysine	SigmaAldrich	P2636-100MG
Glass-bottom petri-dishes	Cellvis	D29-20-1.5-N
Recombinant DNA		
Plasmid: pGEX4T-2	Cytiva	28-9545-50
Plasmid: pGEX4T-2 GST- Mint1(226-314)(MID)	This study	N/A
Plasmid: pGEX4T-2 GST- Mint1(261-272)	This study	N/A
Plasmid: pGEX4T-2 GST- Mint1(261-282)	This study	N/A
Plasmid: pGEX4T-2 GST- Mint1(226-289)	This study	N/A
Plasmid: pGEX4T-2 GST- Mint1(222-314)	This study	N/A
Plasmid: pGEX4T-2 GST- Mint1(237-289)	This study	N/A
Plasmid: pcDNA3.1-N-eGFP Mint1-GFP	This study	N/A
Plasmid: pcDNA3.1-N-eGFP Mint1(D269A/I270A)-GFP	This study	N/A
Plasmid: pET24a(+) Sx1a$_{1-261}$-His	(Christie *et al*, 2012)	N/A
Plasmid: pET28a(+) Munc18-1-His	(Hu *et al.*, 2011)	N/A
Plasmid: pET28a(+) Munc18-1$^{\Delta 317-333}$-His	(Martin *et al.*, 2013)	N/A
pEGFP-N1	Clontec	6085-1
pmEos3.2-N1 Munc18-1^{WT}	This study	N/A
pmEos3.2-N1 Munc18-1^{R388A}	This study	N/A
pCI VAMP2-pHluorin	(Miesenbock *et al.*, 1998)	N/A
Deposited Data		
Minc18-1/Mint1/Sx1 complex (crystal structure)	RSCB Protein Data Bank	PDB ID: 7XSJ
Human Mint1 (protein sequence)	Uniprot	Q02410-1
Human Mint1 (open reading frame)	Genscript	NM_001163.3
Rat Munc18-1 (protein sequence)	Uniprot	P61765-1
Human Sx1a (protein sequence	Uniprot	Q16623-1

Human Mint1 interactome	BioGrid	https://thebiogrid.org/106817/summary/homo-sapiens/apba1.html
Human Mint2 interactome	BioGrid	https://thebiogrid.org/106818/summary/homo-sapiens/apba2.html
Software		
Pymol	Schrodinger, USA.	https://pymol.org/2/
BioGrid4.4.217	(Oughtred *et al.*, 2021)	https://thebiogrid.org
Consurf	(Ashkenazy *et al.*, 2016)	https://consurf.tau.ac.il/consurf_index.php
AlphaFold2 Multimer	(Evans *et al.*, 2022; Jumper *et al.*, 2021)	https://github.com/deepmind/alphafold
ColabFold and ColabFold batch	(Mirdita *et al.*, 2022)	https://github.com/sokrypton/ColabFold
Fiji/ImageJ (version 2.9.0)	(Schneider *et al*, 2012)	https://imagej.net/software/fiji/downloads
Python 3.8	N/A	https://www.python.org/downloads/release/python-380/
DBSCAN	(Schubert *et al*, 2017)	https://scikit-learn.org/stable/modules/generated/sklearn.cluster.DBSCAN.html
Other		
Superose6 Increase10/300 GL	GE Healthcare	Catalogue: 29091596
HiLoad™ Superdex75 PG	GE Healthcare	Catalogue: 28989333

1257 **Table S1. Putative interactors of human Mint1 from BioGRID[a].**

1258

Uniprot Entry ID	Gene Names	AlphaFold predicted Interactor?[c]	Predicted interacting domains	References providing additional validation[b]
O14639	ABLIM1 ABLIM KIAA0059 LIMAB1	-		
Q15067	ACOX1 ACOX	-		
Q9Y2T2	AP3M1	+	C-terminal β-sandwich platform domain of AP3 μ3 subunit binds YxxΦ motif in Mint1	
P05067	APP A4 AD1	+	APP motif binds Mint1 PTB domain.	(Biederer *et al.*, 2002; Borg *et al.*, 1996; Matos *et al.*, 2012; Sakuma *et al.*, 2009; Xie *et al.*, 2013; Zhang *et al.*, 1997)
P61204	ARF3	+	ARF3 small GTPase binds Mint1 PDZ1-PDZ2 tandem domains.	(Hill *et al.*, 2003)
P18085	ARF4	-	ARF4 small GTPase binds Mint1 PDZ1-PDZ2 tandem domains.	(Hill *et al.*, 2003)
Q96DR7	ARHGEF26 SGEF HMFN1864	-		
Q9NXU5	ARL15 ARFRP2	-		
Q9UHR4	BAIAP2L1 IRTKS	-		
Q14012	CAMK1	-		
O14936	CASK LIN2	+	The CaM Kinase domain of CASK binds the CID motif of Mint1	(Borg *et al.*, 1998; Wu *et al.*, 2020; Zhang *et al.*, 2020)
O60563	CCNT1	-		
O14618	CCS	-		(McLoughlin *et al*, 2001)
Q12834	CDC20	-		
Q9P2B7	CFAP97 KIAA1430	-		
Q9Y6M4	CSNK1G3	-		
Q12959	DLG1	-		(Leonoudakis *et al.*, 2004)
P78352	DLG4 PSD95	-		
Q86SJ6	DSG4 CDHF13	-		
Q9H8V3	ECT2	-		
Q9H6Z9	EGLN3	-		
Q8TE02	ELP5 C17orf81 DERP6 HSPC002 MSTP071	-		
Q0PNE2	ELP6 ATP1 C3orf75 TMEM103	-		

P49841	GSK3B	-		
Q9NYZ3	GTSE1	-		
Q8WVV9	HNRNPLL HNRPLL SRRF BLOCK24	-		
P17482	HOXB9 HOX2E	-		
P31274	HOXC9 HOX3B	+	Homeobox domain of HOXC9 binds PTB domain of Mint1	
P28335	HTR2C HTR1C	-		(Becamel *et al*, 2002)
Q14500	KCNJ12 IRK2 KCNJN1	-	KCNJ12 motif binds Mint1 PTB domain.	(Leonoudakis *et al.*, 2004)
O60333	KIF1B KIAA0591 KIAA1448	-		
O00139	KIF2A KIF2 KNS2	-		
O95198	KLHL2	-		
Q6TFL4	KLHL24 DRE1	-		
Q9NS86	LANCL2 GPR69B TASP	-		
Q9UGP4	LIMD1	-		
O14910	LIN7A MALS1 VELI1	-		
Q9HAP6	LIN7B MALS2 VELI2 UNQ3116/PRO10200	-		(Leonoudakis *et al.*, 2004)
Q9NUP9	LIN7C MALS3 VELI3	-		(Leonoudakis *et al.*, 2004)
Q14114	LRP8 APOER2	+	LRP8 motif binds Mint2 PTB domain.	(He *et al.*, 2007)
Q9P0L2	MARK1 KIAA1477 MARK	-		
Q7L590	MCM10 PRO2249	-		
Q9BTE3	MCMBP C10orf119	-		
Q8WV92	MITD1	-		
P61764	Munc18-1 STXBP1 UNC18A	+	Munc18-1 domain3a binds Mint1 AHM.	(Biederer & Sudhof, 2000; Graham *et al.*, 2011; Han *et al.*, 2014; Ho *et al.*, 2002b; Li *et al.*, 2023; Okamoto & Sudhof, 1997, 1998; Park *et al.*, 2012). This study.
Q7Z628	NET1 ARHGEF8	-		
Q12986	NFX1 NFX2	-		
P52952	NKX2-5 CSX NKX2.5 NKX2E	-		
Q9BW91	NUDT9 NUDT10 PSEC0099 UNQ3012/PRO9771	-		
O95747	OXSR1 KIAA1101 OSR1	-		

Q6ZW49	PAXIP1 PAXIP1L PTIP CAGF28	-		
Q13526	PIN1	-		
Q99755	PIP5K1A	-		
Q99569	PKP4	-		
O00411	POLRMT	-		
Q13356	PPIL2	-		
Q9BZL6	PRKD2 PKD2 HSPC187	-		
P49810	PSEN2 AD4 PS2 PSNL2 STM2	-		(Biederer *et al.*, 2002)
Q5TGL8	PXDC1 C6orf145	-		
Q9NW64	RBM22 ZC3H16 199G4	-		
O94761	RECQL4 RECQ4	-		
Q8WVD3	RNF138 NARF HSD-4 HSD4	-		
Q96P16	RPRD1A P15RS	-		
P51812	RPS6KA3 ISPK1 MAPKAPK1B RSK2	-		
Q7L4I2	RSRC2	-		
P33764	S100A3 S100E	-		
Q86UD0	SAPCD2 C9orf140	-		
Q9BXP2	SLC12A9 CCC6 CIP1	-		
Q8N5C6	SRBD1	-		
Q8WVM0	TFB1M CGI-75	-		
Q5JTD0	TJAP1 PILT TJP4	-		
O95985	TOP3B TOP3B1	-		
Q9ULW0	TPX2 C20orf1 C20orf2 DIL2 HCA519	-		
Q8WVR3	TRAPPC14 C7orf43 MAP11	-		
Q9Y296	TRAPPC4 SBDN CGI-104 HSPC172 PTD009	-		
Q96Q05	TRAPPC9 KIAA1882 NIBP T1	-		
Q7Z2T5	TRMT1L C1orf25 TRM1L MSTP070	-		
Q9UPT9	USP22 KIAA1063 USP3L	+	USP domain of USP22 binds Mint1 PDZ1-PDZ2 tandem domains.	
Q8IWA0	WDR75 UTP17	-		
O95785	WIZ ZNF803	+	C-terminal Zinc-finger of WIZ binds the PDZ1-PDZ2 tandem domains of Mint1	
Q86U90	YRDC DRIP3 IRIP	-		
Q8N5A5	ZGPAT GPATC6 GPATCH6 KIAA1847 ZC3H9 ZC3HDC9 ZIP	-		

a. https://thebiogrid.org/106817/summary/homo-sapiens/apba1.html

1262 b. The BioGRID database provides references for each identified putative interaction. These are
1263 typically, although not always, high-throughput proteomics studies. Here we provide citations for
1264 other studies that have provided additional validation using methods such as immunoprecipitation,
1265 *in vitro* binding assays, or macromolecular structure determination.
1266
1267 c. The definition of “Interactor” is based on a semi-quantitative measure of the AlphaFold2-derived
1268 interfacial PTM (iPTM) score, visual inspection of the resultant PAE graphs and assessment of the
1269 structure in PyMOL. After generating single multimer predictions in AlphaFold2 in unsupervised
1270 batch mode, we found that a minimum iPTM score of 0.3 combined with a strong signal in the PAE
1271 plot for inter-molecular structural correlation provided a useful indicator for structural predictions for
1272 further assessment. In these cases, we then ran three independent modelling experiments to assess
1273 whether multiple predictions resulted in consistent structural alignments in PyMOL.
1274

1275 **Table S2. Putative interactors of human Mint2 from BioGRID[a].**

1276

Uniprot Entry ID	Gene Names	AlphaFold predicted Interactor?[c]	Predicted interacting domains	References providing additional validation[b]
Q6PD74	AAGAB	-		
Q9UBZ4	APEX2 APE2 APEXL2 XTH2	-		
P05067	APP A4 AD1	+	APP motif binds Mint2 PTB domain.	(Borg *et al.*, 1996; Matos *et al.*, 2012; Xie *et al.*, 2013; Zhang *et al.*, 1997)
P61204	ARF3	+	ARF3 small GTPase binds Mint2 PDZ1-PDZ2 tandem domains.	(Hill *et al.*, 2003)
P18085	ARF4	+	ARF4 small GTPase binds Mint2 PDZ1-PDZ2 tandem domains.	(Hill *et al.*, 2003)
Q7Z3C6	ATG9A APG9L1	-		
O15155	BET1	-		
Q9Y297	BTRC BTRCP FBW1A FBXW1A	-		
A6NLJ0	C2CD4B FAM148B NLF2	-		
O94985	CLSTN1 CS1 KIAA0911	+	CLSTN1 motif binds Mint2 PTB domain.	(Araki *et al.*, 2003)
Q9GZR7	DDX24	-		
Q09019	DMWD DM9	-		
Q9UKB1	FBXW11 BTRCP2 FBW1B FBXW1B KIAA0696	-		
A4D1S0	KLRG2 CLEC15B	-		
Q07954	LRP1 A2MR APR	+	LRP1 motif binds Mint2 PTB domain.	(Gotthardt *et al.*, 2000)
P98164	LRP2	+	LRP2 motif binds Mint2 PTB domain.	(Gotthardt *et al.*, 2000)
Q14114	LRP8 APOER2	+	LRP8 motif binds Mint2 PTB domain.	(Gotthardt *et al.*, 2000)
Q8N7X4	MAGEB6	-		
Q16659	MAPK6 ERK3 PRKM6	-		

P61764	Munc18-1 STXBP1 UNC18A	+	Munc18-1 domain3a binds Mint2 AHM.	(Biederer & Sudhof, 2000; Graham *et al.*, 2011; Han *et al.*, 2014; Ho *et al.*, 2002b; Li *et al.*, 2023; Okamoto & Sudhof, 1997, 1998; Park *et al.*, 2012). This study.
Q96P71	NECAB3 APBA2BP NIP1 SYTIP2 XB51	-		(Lee *et al*, 2000)
Q13393	PLD1	-		
P49810	PSEN2 AD4 PS2 PSNL2 STM2	-		(Biederer *et al.*, 2002)
O94761	RECQL4 RECQ4	-		
Q04206	RELA NFKB3	-		(Tomita *et al*, 2000)
Q9NVW2	RLIM RNF12	-		
Q68DV7	RNF43	-		
O15431	SLC31A1 COPT1 CTR1	-		
Q9HB58	SP110	-		
Q8N9I0	SYT2	-		
Q5JTD0	TJAP1 PILT TJP4	+	TJAP1 N-terminal sequence binds Mint2 PTB domain in non-canonical site	
Q8NFZ5	TNIP2 ABIN2 FLIP1	-		
Q8WV44	TRIM41 RINCK	-		
Q9Y2K6	USP20 KIAA1003 LSFR3A VDU2	-		
Q8TEY7	USP33 KIAA1097 VDU1	-		
Q6AHZ1	ZNF518A KIAA0335 ZNF518	-		

a. https://thebiogrid.org/106818/summary/homo-sapiens/apba2.html

b. The BioGRID database provides references for each identified putative interaction. These are typically, although not always, high-throughput proteomics studies. Here we provide citations for

other studies that have provided additional validation using methods such as immunoprecipitation, *in vitro* binding assays, or macromolecular structure determination.

c. The definition of “Interactor” is based on a semi-quantitative measure of the AlphaFold2-derived interfacial PTM (iPTM) score, visual inspection of the resultant PAE graphs and assessment of the structure in PyMOL. After generating single multimer predictions in AlphaFold2 in unsupervised batch mode, we found that a minimum iPTM score of 0.3 combined with a strong signal in the PAE plot for inter-molecular structural correlation provided a useful indicator for structural predictions for further assessment. In these cases, we then ran three independent modelling experiments to assess whether multiple predictions resulted in consistent structural alignments in PyMOL.

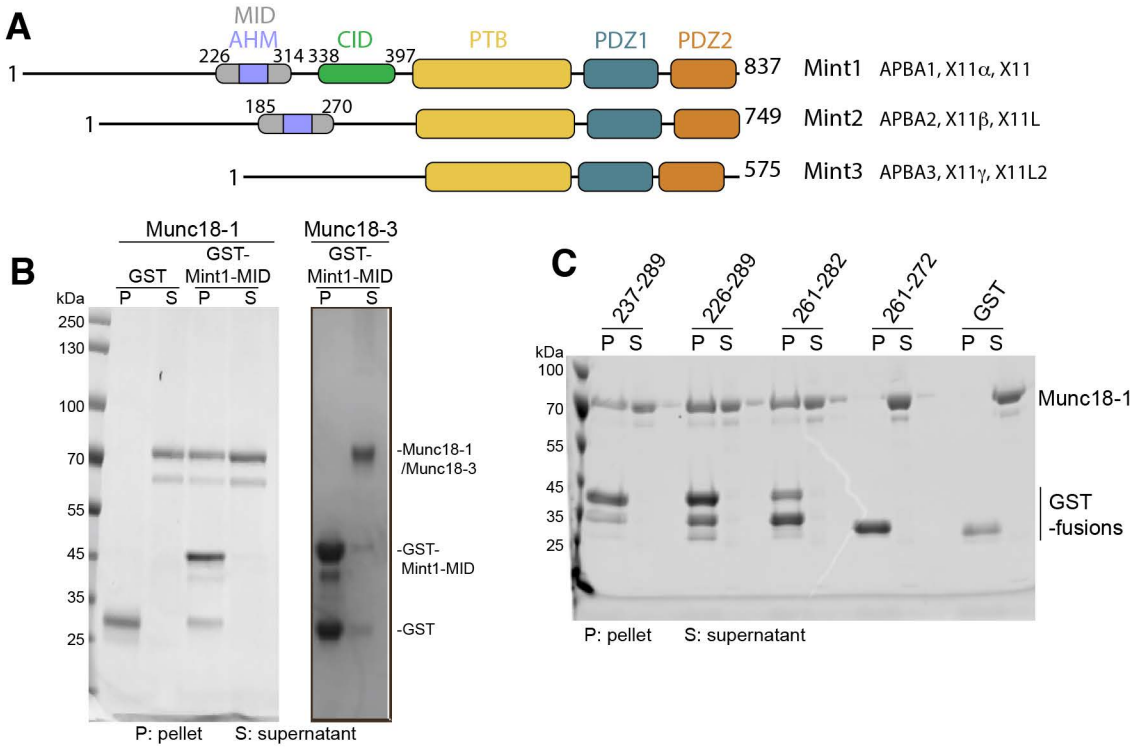

Figure 1. The Mint1 MID interacts directly with Munc18-1 but not Munc18-3
(A) Schematic diagram of the human Mint proteins. (AHM, acidic α-heilcal motif; MID, Munc18-1-interacting domain; CID, CASK interacting domain; PTB, phosphotyrosine binding domain; PDZ1 and PDZ2, Psd95/Dlg/ZO1 domains). (B) Pulldowns with GST-Mint1 MID show a direct interaction with purified Munc18-1 but not Munc18-3. Image shows Coomassie Blue stained gel. (C) Pulldowns with GST-tagged Mint1 truncated sequences identify residues 261-282 as sufficient and required for Munc18-1 binding. Image shows Coomassie Blue stained gel.

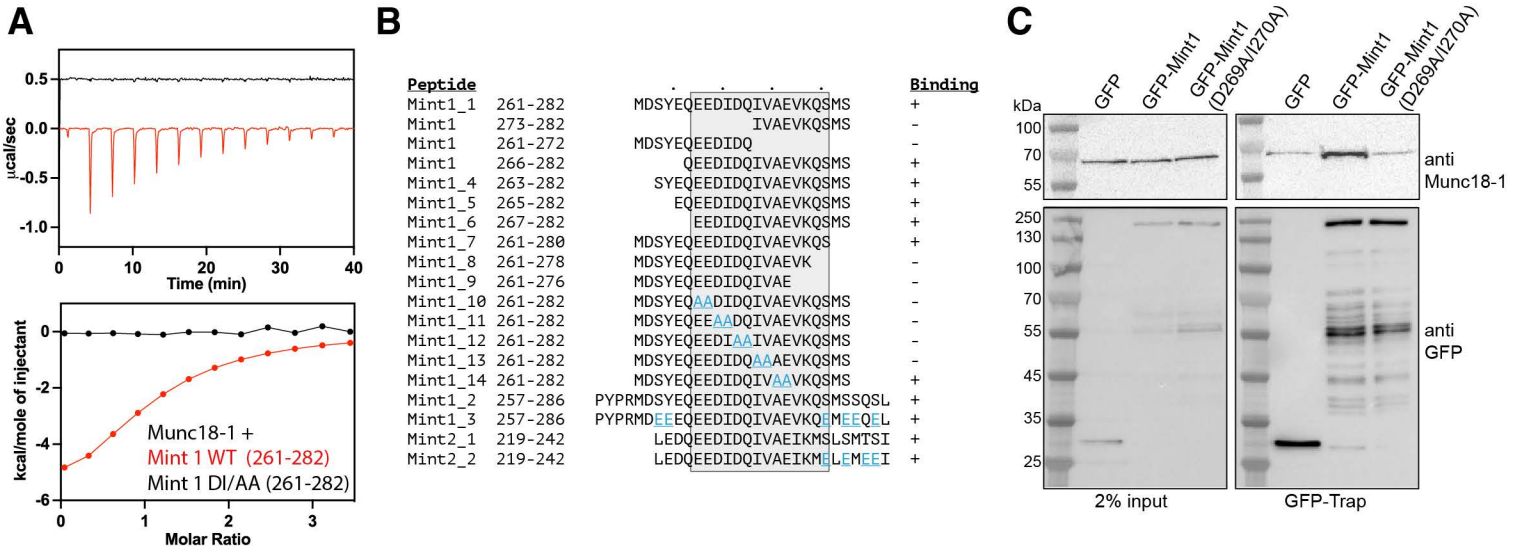

Figure 2. A conserved sequence in Mint1 and Mint2 binds Munc18-1 and is not influenced by phosphorylation
(A) ITC of synthetic Mint1261-282 peptide binding to purified Munc18-1. The top shows raw ITC data, and the bottom shows integrated and normalised data fit to a 1:1 binding model. (B) Sequences of peptides tested for Munc18-1 binding by ITC. The minimal and highly conserved sequence required for Munc18-1 binding is shaded. Mutated peptide residues are highlighted in blue. (C) Endogenous Munc18-1 is bound to GFP-tagged Mint1 but not the mutant GFP-Mint1D269A/I270A. GFP-tagged Mint1 proteins were transiently transfected into PC12 cells, immunoprecipitated with GFP-nanobody coupled beads, and the bound proteins probed by Western blot with anti-Munc18-1.

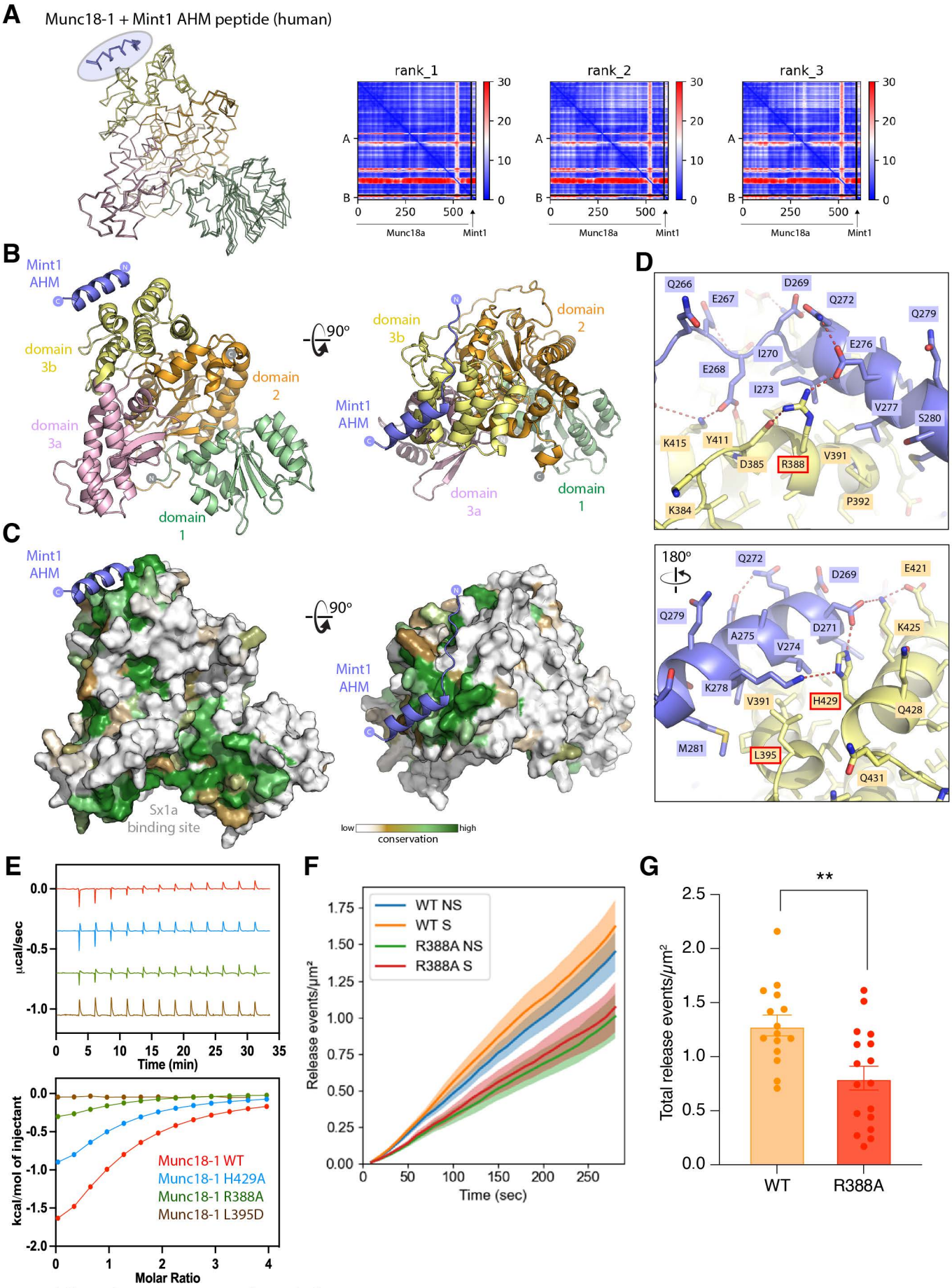

Figure 3. Modelling of Munc18-1 in complex with the Mint1 AHM sequence.
(A) AlphaFold2 prediction of the complex between Munc18-1 and Mint1 AHM. The three top ranked models are overlaid and shown in backbone ribbon representation. The AHM is consistently modelled in an α-helical structure associated with the Munc18-1 domain3b (highlighted in blue). On the right the predicted alignment error (PAE) is plotted for each model. Signals in the off-diagonal regions indicate strong structural correlations between residues in the peptide with the Munc18-1 protein. Fig. S4 shows predictions of the full-length Munc18-1 and Mint1 complex as well as models of other Munc and Mint homologues and orthologues. (B) The top-ranked complex of Munc18-1 and the Mint1 AHM is shown in cartoon representation, with Munc18-1 domains highlighted. (C) As in (B) but the surface of Munc18-1 is shown coloured for sequence conservation as calculated by Consurf (Ashkenazy et al., 2016). (D) Opposite views showing details of the Mint1 AHM bound to the Munc18-1 domain3b. (E) ITC of synthetic Mint1(261-282) peptide binding to purified Munc18-1 and structure-based mutants. The top shows raw ITC data, and the bottom shows integrated and normalised data fit to a 1:1 binding model. Mutated residues are highlighted in panel (D). (F) Cumulative release events over time for each data group was analysed and the number of release events at each 10 sec interval from 0-290 sec was determined, plotted as MEAN±SEM. (G) Total evoked release events following stimulation were measured per µm2. Non-parametric Mann Whitney U test, $p < 0.05$, *, $p < 0.01$. N = 15 cells (WT) and 17 (R388A) from independent experiments.

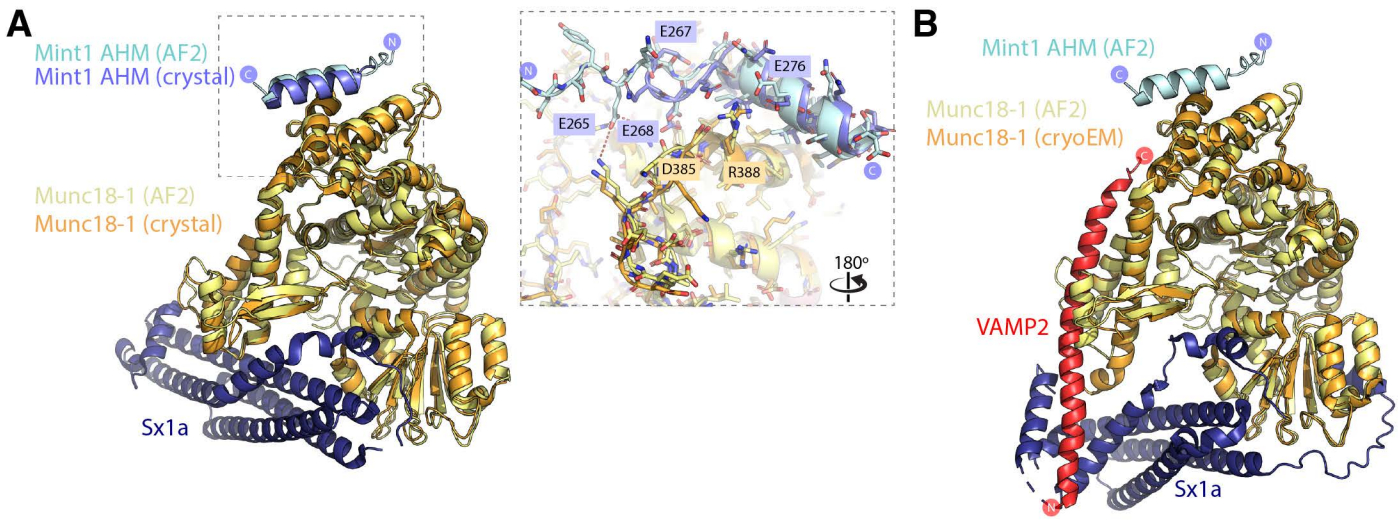

Figure 4. Comparison of the predicted Munc18-1/Mint1 complex with experimental structures.
(A) Overlay of the Munc18-1 complex with Mint1 AHM predicted by AlphaFold2 and the recent crystal structure of the Munc18-1/Sx-1a/Mint1 complex (Li et al., 2023). The inset shows details of the binding site modelled by AlphaFold2 and observed in the crystal structure. The two structures are identical in all key respects. (B) Overlay of the Munc18-1 complex with Mint1 AHM predicted by AlphaFold2 and the cryoEM structure of the Munc18-1/Sx1a/VAMP2 complex (Stepien et al., 2022). The Mint1 AHM is expected to bind Munc18-1 independently of the Sxa1 t-SNARE and VAMP2 v-SNARE proteins.

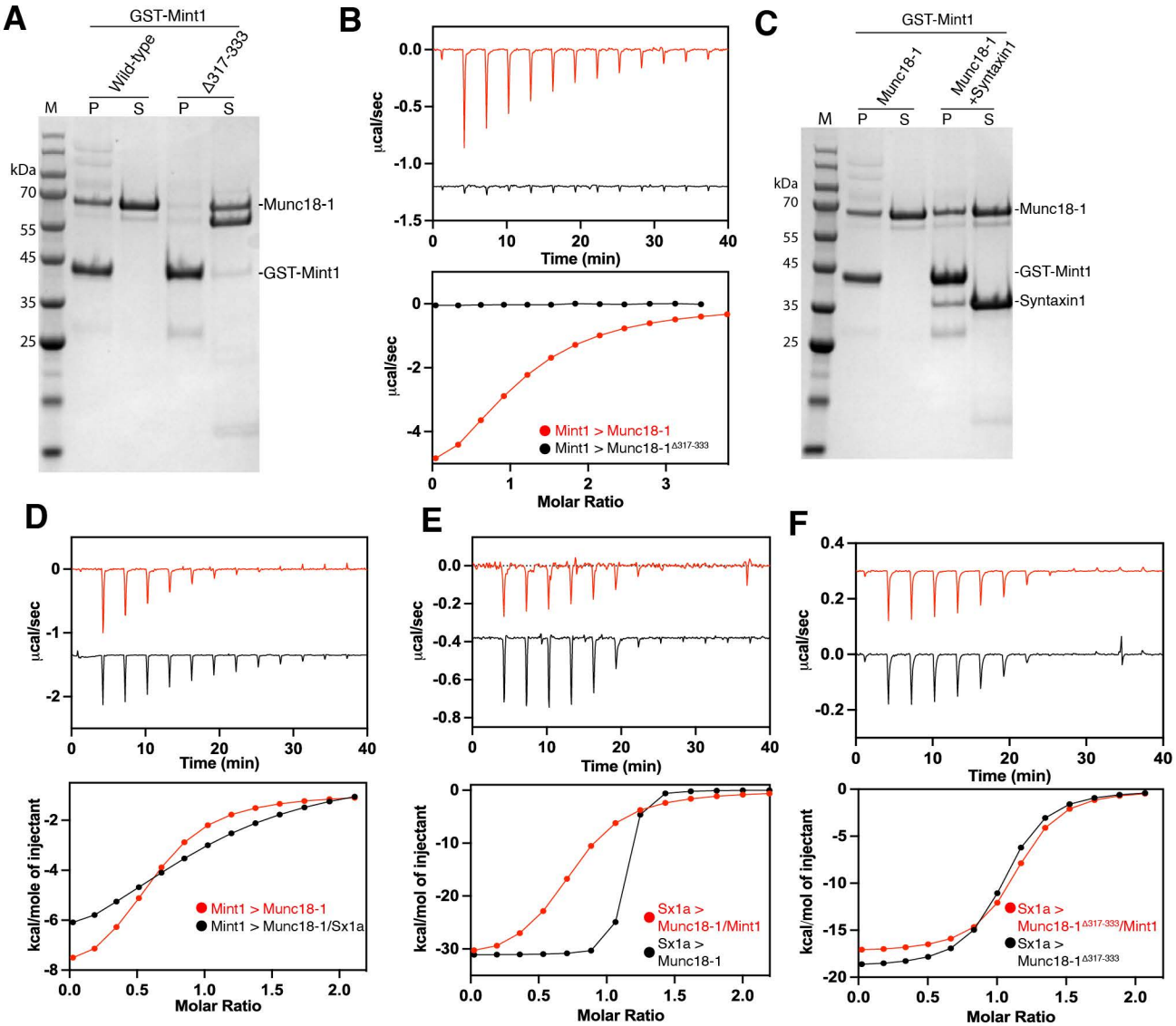

Figure 5. Mint1 and Sx1a show allosteric effects on binding to Munc18-1

(A) Pulldowns with GST-Mint1 MID show that Munc18-1 domain3a hinge loop is important for binding. As Mint1 does not contact domain3a this suggests an allosteric effect on the domain3b binding site. Image shows Coomassie stained gel. (B) ITC of synthetic Mint1261-282 peptide binding to purified Munc18-1 (red) and Munc18-1Δ317-333 (black) confirm the requirement of domain3a for Mint1 interaction. (C) Pulldowns with GST-Mint1 MID show that Mint1 can bind Munc18-1 both alone and in the presence of Sx1a. Image shows Coomassie stained gel. (D) Although Mint1 and Sx1a can bind Munc18 simultaneously, ITC of Mint1 Mint1261-282 AHM peptide binding to Munc18-1 in the absence (red) and presence (black) of Sx1a shows a reduction in binding affinity and enthalpy. (E) ITC of Sx1a binding to Munc18-1 in the absence (black) and presence (red) of synthetic Mint1261-282 peptide. Together this shows there is a subtle allosteric inhibition of Sxa1 binding to Munc18-1 in the presence of Mint1. (F) ITC of Sx1a binding to Munc18-1Δ317-333 in the absence (black) and presence (red) of synthetic Mint1261-282 peptide.

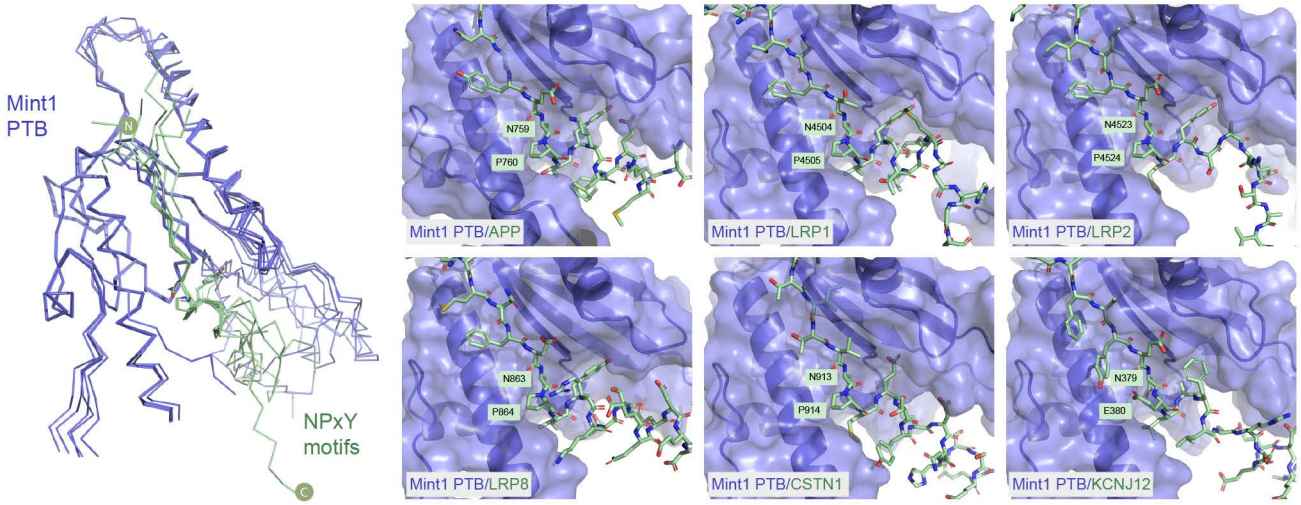

Figure 6. Interactions of the Mint PTB domains with canonical NPxY-containing peptide motifs predicted by AlphaFold2
Overlay of the top-ranked AlphaFold2 predicted structures of the Mint1 PTB domain (blue) in complex with various NPxY-related peptide motifs (green) shown in backbone ribbon representation. These sequences are predicted to bind the canonical binding groove of the PTB domain (with similar interactions predicted for Mint2 (not shown)). The right panel shows details of the different sequences derived from various Mint-interacting transmembrane proteins.

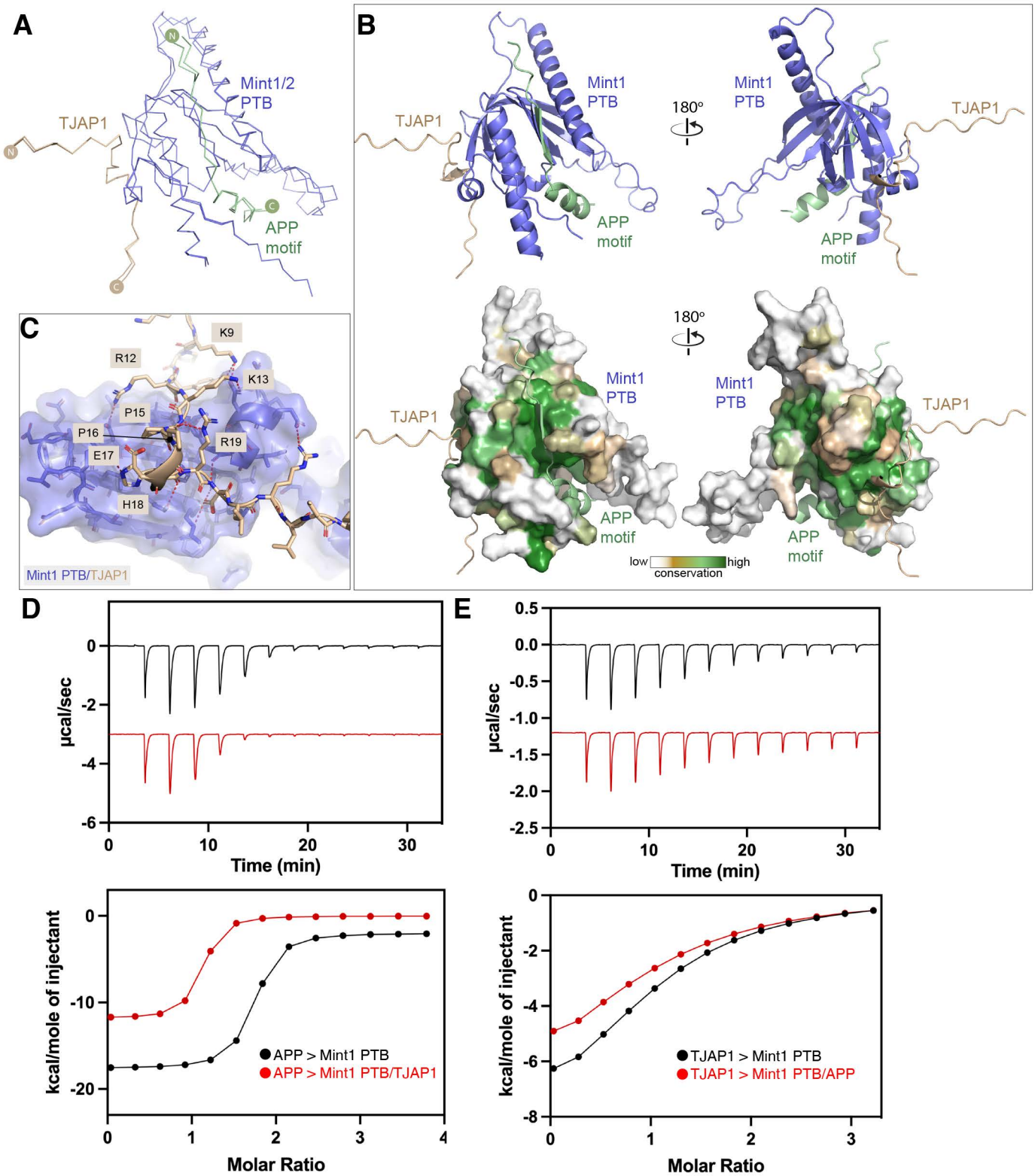

Figure 7. Interactions of the Mint PTB domains with a non-canonical peptide motif from TJAP1 predicted by AlphaFold2
(A) Overlay of the top-ranked AlphaFold2 predicted structures of the Mint1 and Mint2 PTB domains (blue) in complex with the APP NPxY motif (green) and the N-terminal peptide of TJAP1 (brown) shown in backbone ribbon representation. (B) The top-ranked complex of Mint1 PTB domain bound to APP and TJAP1 is shown in cartoon representation. The lower panel shows the surface of Mint1 coloured for sequence conservation as calculated by Consurf (Ashkenazy et al., 2016). (C) Details of the Mint1 PTB domain interaction with the TJAP1 peptide. (D) ITC of Mint1 PTB binding to the peptide motif from APP in the presence and absence of a peptide from TJAP1. (E) ITC of Mint1 PTB binding to the peptide motif from TJAP1 in the presence and absence of a peptide from APP. The top shows raw ITC data, and the bottom shows integrated and normalised data fit to a 1:1 binding model.

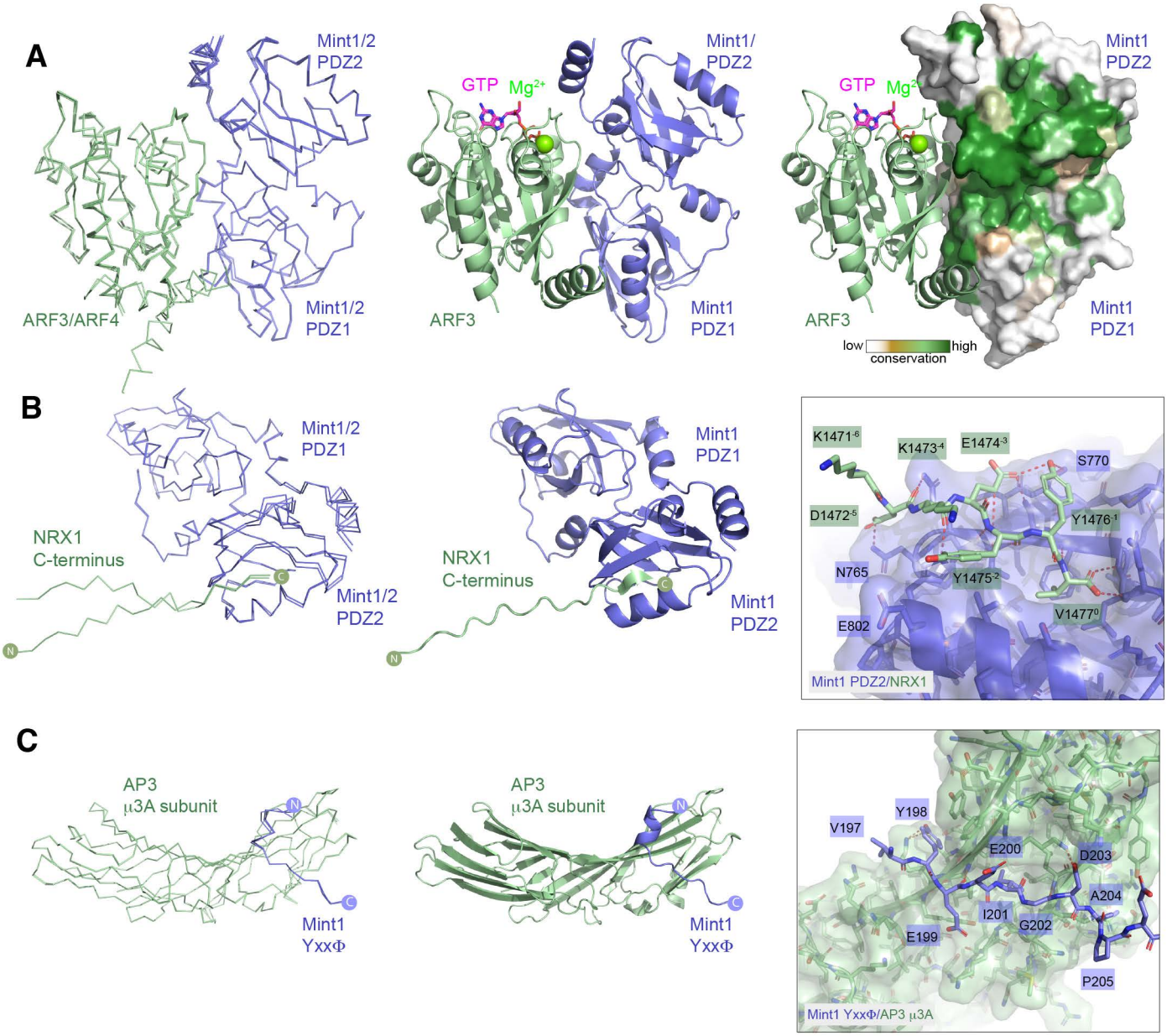

Figure 8. Interactions of the Mint N-terminus and PDZ domains with novel binders predicted by AlphaFold2
(A) Overlay of the top-ranked AlphaFold2 predicted structures of the Mint1 and Mint2 tandem PDZ domains (blue) in complex with ARF3 and ARF4 (green) shown in backbone ribbon representation. The middle panel shows the Mint1 complex with ARF3 in ribbon representation, with the position of GTP and Mg2+ based on the previous crystal structure of active ARF3-GTP (Lee et al., 2019). The right panel shows the same image but with Mint1 surface coloured for sequence conservation as calculated by Consurf (Ashkenazy et al., 2016). (B) Overlay of the top-ranked AlphaFold2 predicted structures of the Mint1 and Mint2 tandem PDZ domains (blue) in complex with the C-terminal PDZbm of NRX1 (green) shown in backbone ribbon representation. The middle panel shows the Mint1 complex with ARF3 in ribbon representation. The right panel inset shows the details of the NRX1 interaction with Mint1 PDZ2 domain. (C) Overlay of the top three ranked AlphaFold2 predicted structures of the Mint1 Yxxϕ motif (blue) in complex with the C-terminal MHD of the AP3 μ3A subunit (green) shown in backbone ribbon representation. The middle panel shows the Mint1 complex with μ3A in ribbon representation. The right panel inset shows the details of the Mint1 Yxxϕ motif interaction with μ3A.

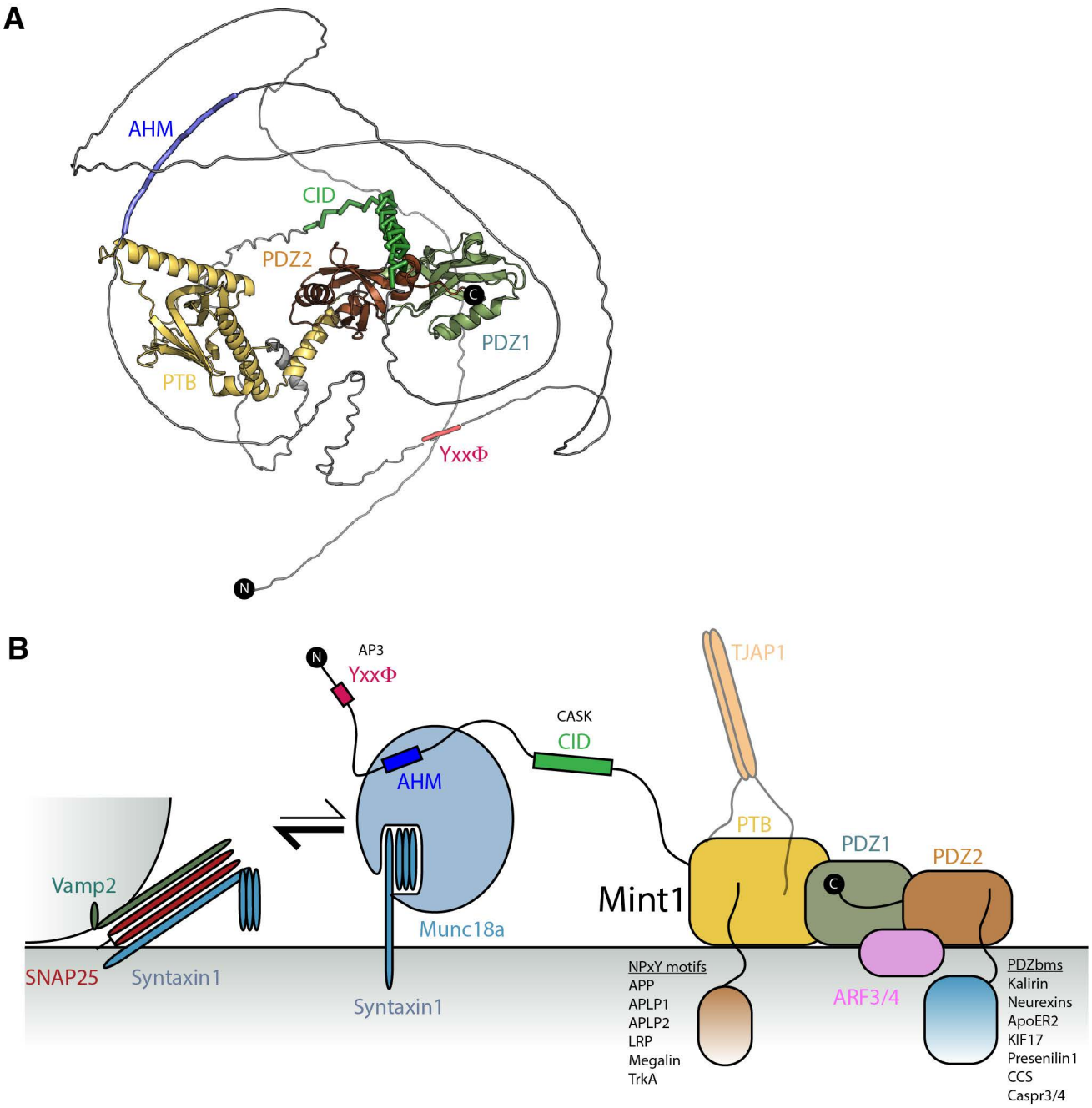

Figure 9. Mint1 structural model and interactions.
(A) Structural model of Mint1 derived from AlphaFold2 (Ammann et al., 2016). (B) Schematic summary of Mint1-mediated interactions, and speculative model suggesting that at the cell surface Mint1 may act to reduce the affinity of Munc18-1 for the auto-inhibited Sx1a, thus enhancing the ability of Sx1a to associate with VAMP2 and SNAP25 to form the trans-SNARE assembly required for vesicle fusion. The C-terminal domains of Mint1 in contrast are associated with other proteins containing NPxY and PDZbm sequences and ARF small GTPases that may enhance Mint1 membrane recruitment and modulate transmembrane protein trafficking.

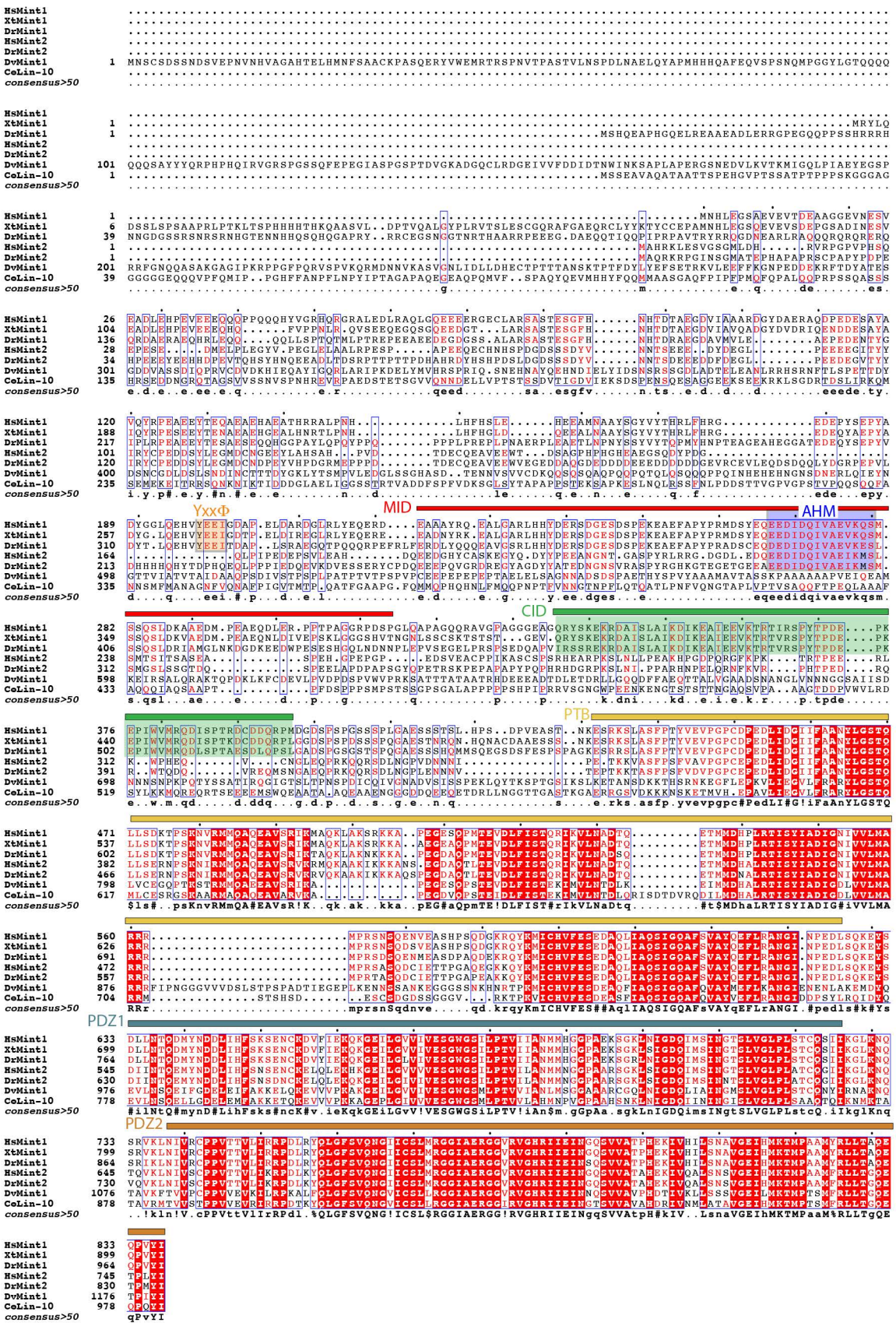

Figure S1. Sequence alignment of Mint proteins. (Related to Fig. 1)
(A) Sequence alignment Mint1 and Mint2. Alignment was performed with Multalin (Corpet et al., 1999) and rendered with ESPript3.0 (Robert and Gouet, 2014). Hs, Homo sapiens. Xt, Xenopus tropicalis. Dr, Danio rerio. Ce, Caenorhabditis elegans. Dv, Drosophila virilis.

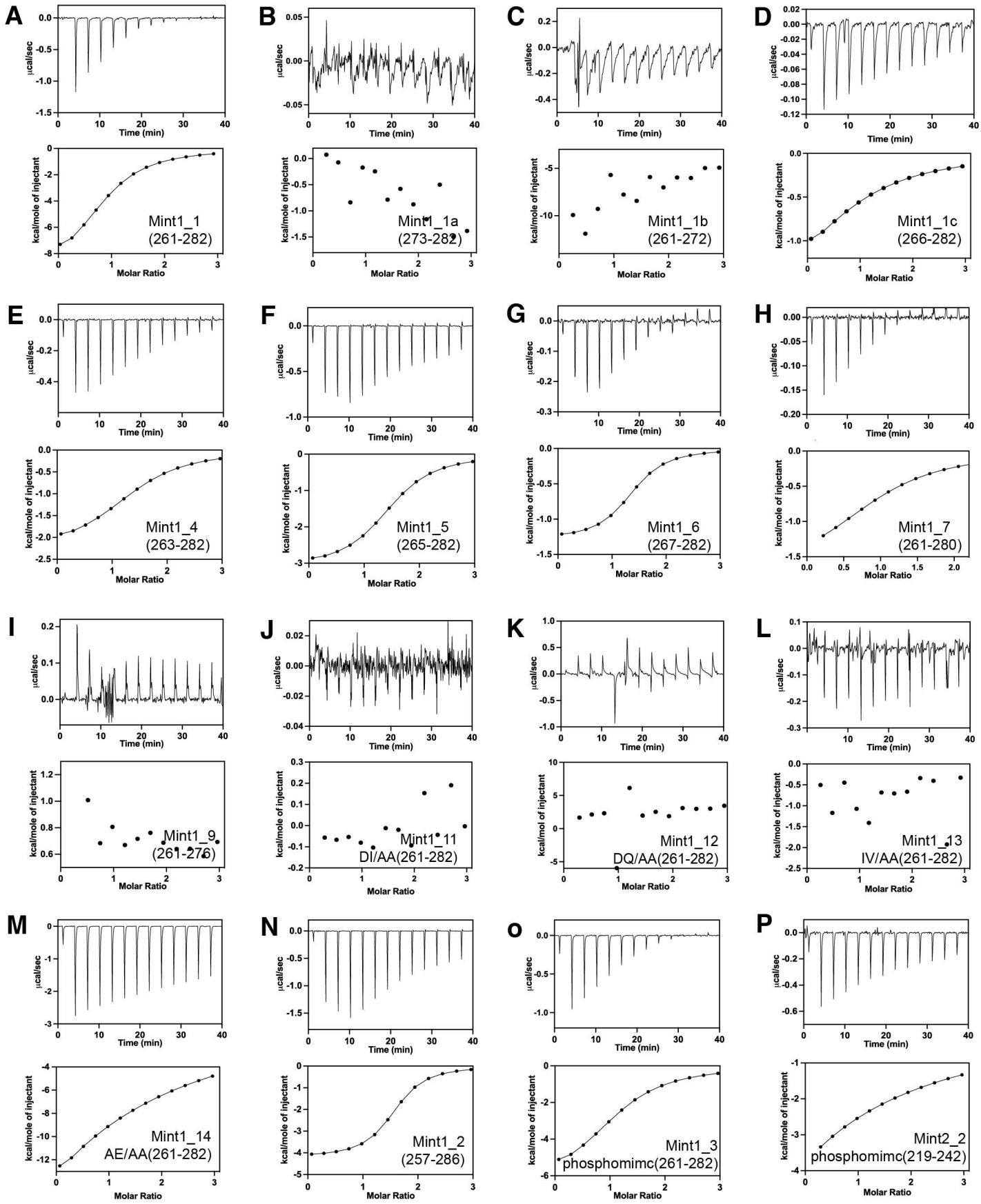

Figure S2. ITC experiments of Munc18-1 binding to various Mint peptides. (Related to Fig. 2)
Example ITC experiments are shown for each of the Mint peptides binding to Munc18-1 as described in Fig. 2B and Table 1. (A) Mint 1_1 (261-282) (B) Mint 1_1a (273-282) (C) Mint 1_1b (261-272) (D) Mint 1_1c (266-282) (E) Mint 1_4 (263-282) (F) Mint 1_5 (265-282) (G) Mint 1_6 (267-282) (H) Mint 1_7 (261-280) (I) Mint 1_9 (261-276) (J) Mint 1_11 DI /AA (261-282 (K) Mint 1-12 DQ /AA (261-282) (L) Mint 1_13 IV/AA(261-282) (M) Mint 1_14 AE/AA(261-282) (N) Mint 1_2 (257-286) (o) Mint 1_3 phosphomimetic (261-282) (P) Mint 2_2 phosphomimetic (219-242)

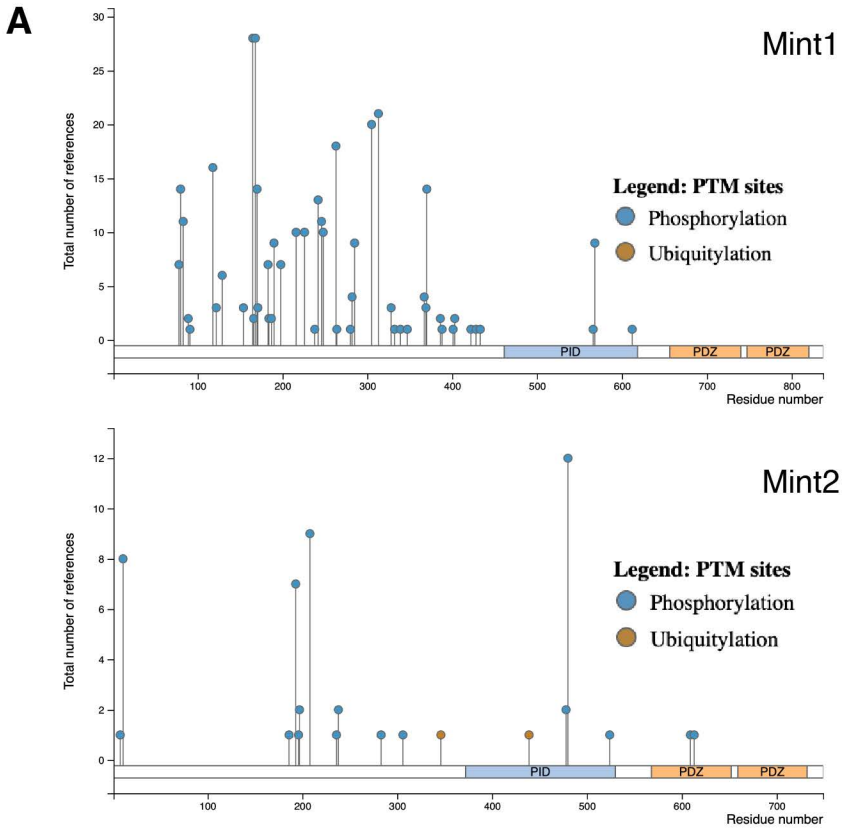

B

phosphorylation

```
hMint1  237-HYDERSDGESDSPEKEAEFAPYPRMDSYEQEEDIDQIVAEVKQSMSSQSLDKAAEDM
hMint2  193-YQDYYPEEANGNTGASPYRLRRGDGDLEDQEEDIDQIVAEIKMSLSMTSITSASEAS
                                          Munc18-binding
```

C

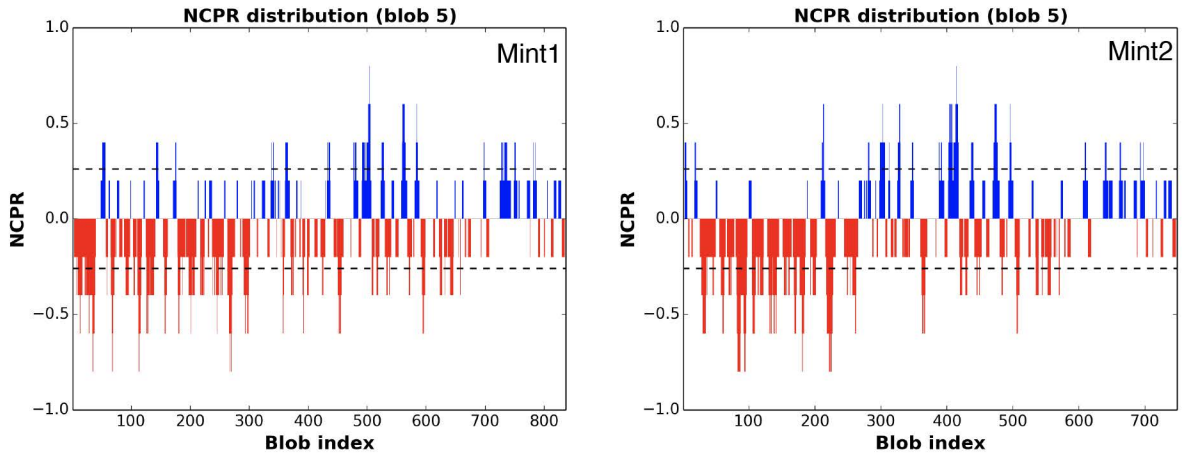

Figure S3. Post-translational modifications and sequence charge distribution of human Mint1 and Mint2. (Related to Fig. 2)
(A) Sites of phosphorylation and ubiquitination of human Mint1 and Mint2 experimentally observed and reported in PhosphoSitePlus (Hornbeck et al., 2015). (B) Phosphorylation sites in the human Mint1 and Mint2 N-terminal regions documented in PhosphoSitePlus (Hornbeck et al., 2015). Phosphomimetic mutations in regions adjacent to the Munc18-1 binding sequence do not influence affinity (Fig. 2B; Table 1). (C) Plot of the charge distribution versus the sequence of Mint1 and Mint2 shows that the N-terminal disordered sequences have a high net-positive charge. Plots were made with CIDER (Holehouse et al., 2015).

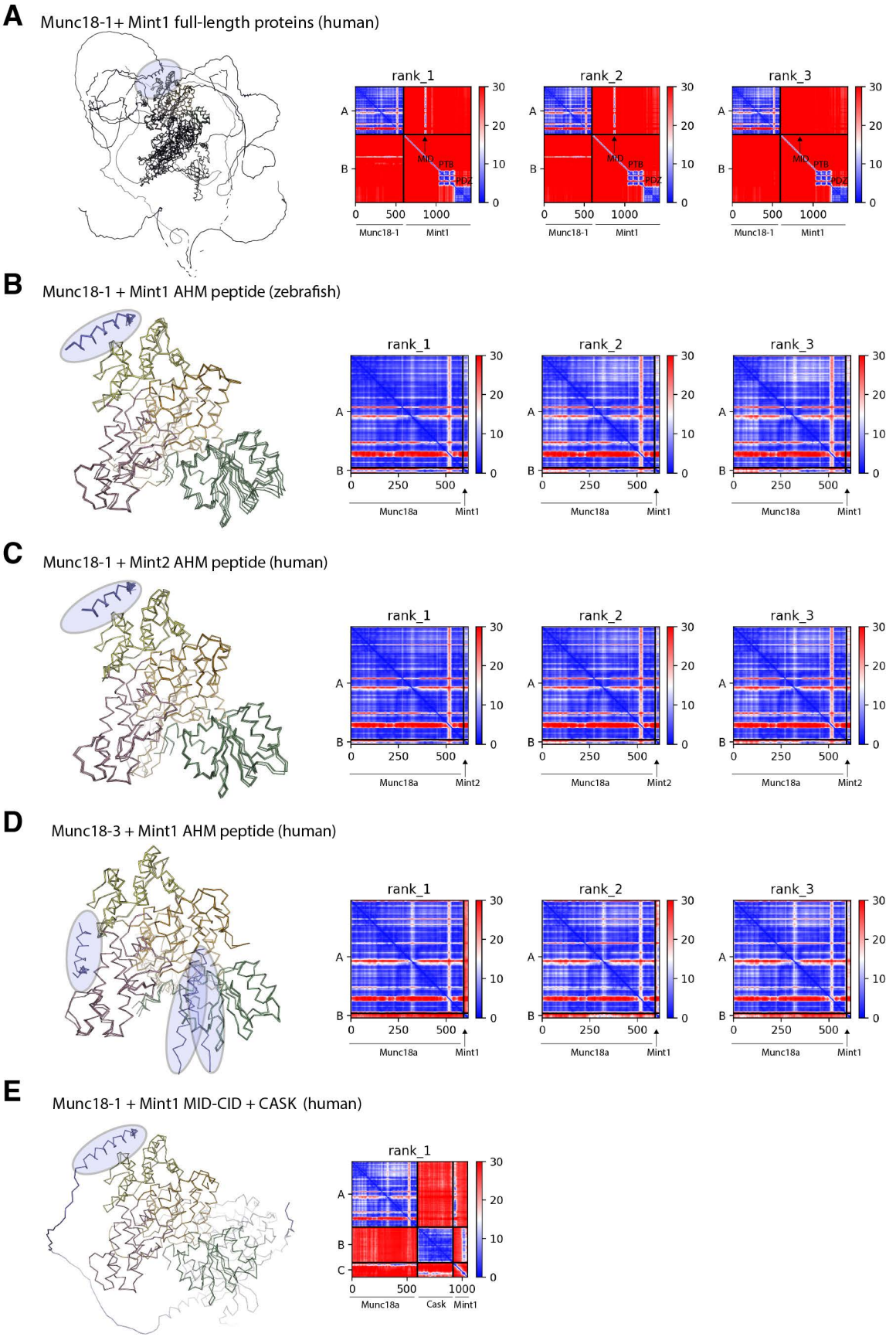

Figure S4. AlphaFold2 modelling of Munc18 interactions with Mint1. (Related to Fig. 3)
(A) Overlaid top three ranked models of human Mint1 bound to Munc18-1 from ColabFold shown in backbone ribbon representation. Mint1 is consistently modelled to bind Munc18-1 domain 3b via a short acidic α-helical motif (AHM) within its unstructured N-terminal domain (highlighted in blue). On the right hand side the predicted alignment error (PAE) is plotted for each model. Signals in the off-diagonal regions indicate strong structural correlations between residues in the peptide with the Munc18-1 protein. (B) Overlaid top three ranked models of the zebrafish Mint1 AHM sequence bound to Munc18-1 predicted with ColabFold. Similar to the human structures, the AHM is consistently modelled in an α-helical structure associated with the Munc18-1 domain3b (highlighted in blue). (C) Overlaid top three ranked models of the human Mint2 AHM sequence bound to Munc18-1 predicted with ColabFold. (D) Overlaid top three ranked models of the human Mint1 AHM sequence modelled with the non-binding Munc18-3 homologue. The AHM is modelled at several random positions (highlighted in blue). The PAE plots do not show evidence of significant interactions between the two proteins. (E) The top scoring model of the human Mint1 AHM and CID sequences bound to Munc18-1 and CASK using ColabFold. The AHM region is predicted in an identical binding site on Munc18-1 to the isolated peptide sequence (highlighted in blue). The CID sequence is predicted to bind to CASK in almost essentially the same conformation as the two previous crystal structures (Wu et al., 2020; Zhang et al., 2020).

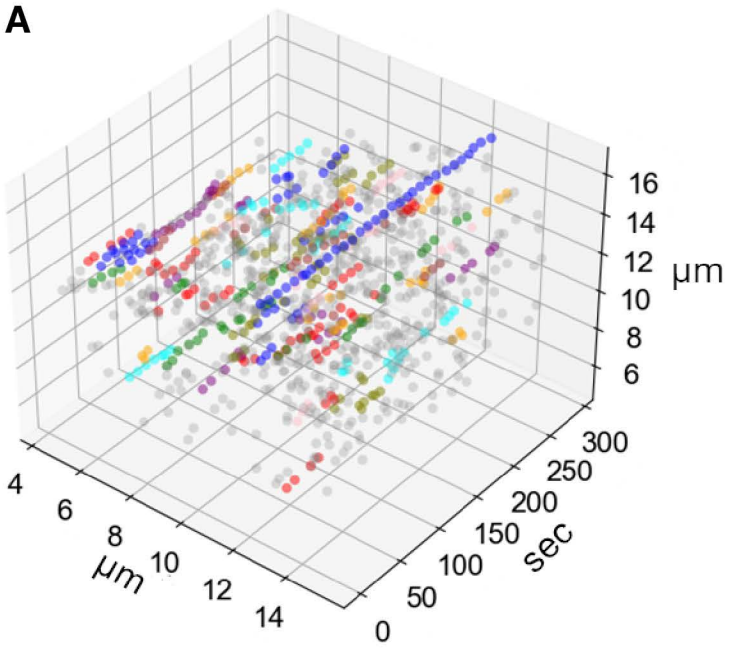

Figure S5. Analysis of cell footprint and fusion events in Munc18 DKO PC3 cells.
(A) Representative fluorescent release event visualisation. The imaging dataset was divided into 10 sec (100 frame) intervals and the fluorescence averaged. Vesicle fusions at each interval were determined by Laplacian of Gaussian and used to create a 3D [x,y,t] array. DBSCAN was used to determine clusters of fluorescent areas/vesicles which persisted in the same area over time. A release event was defined as the end of each cluster.

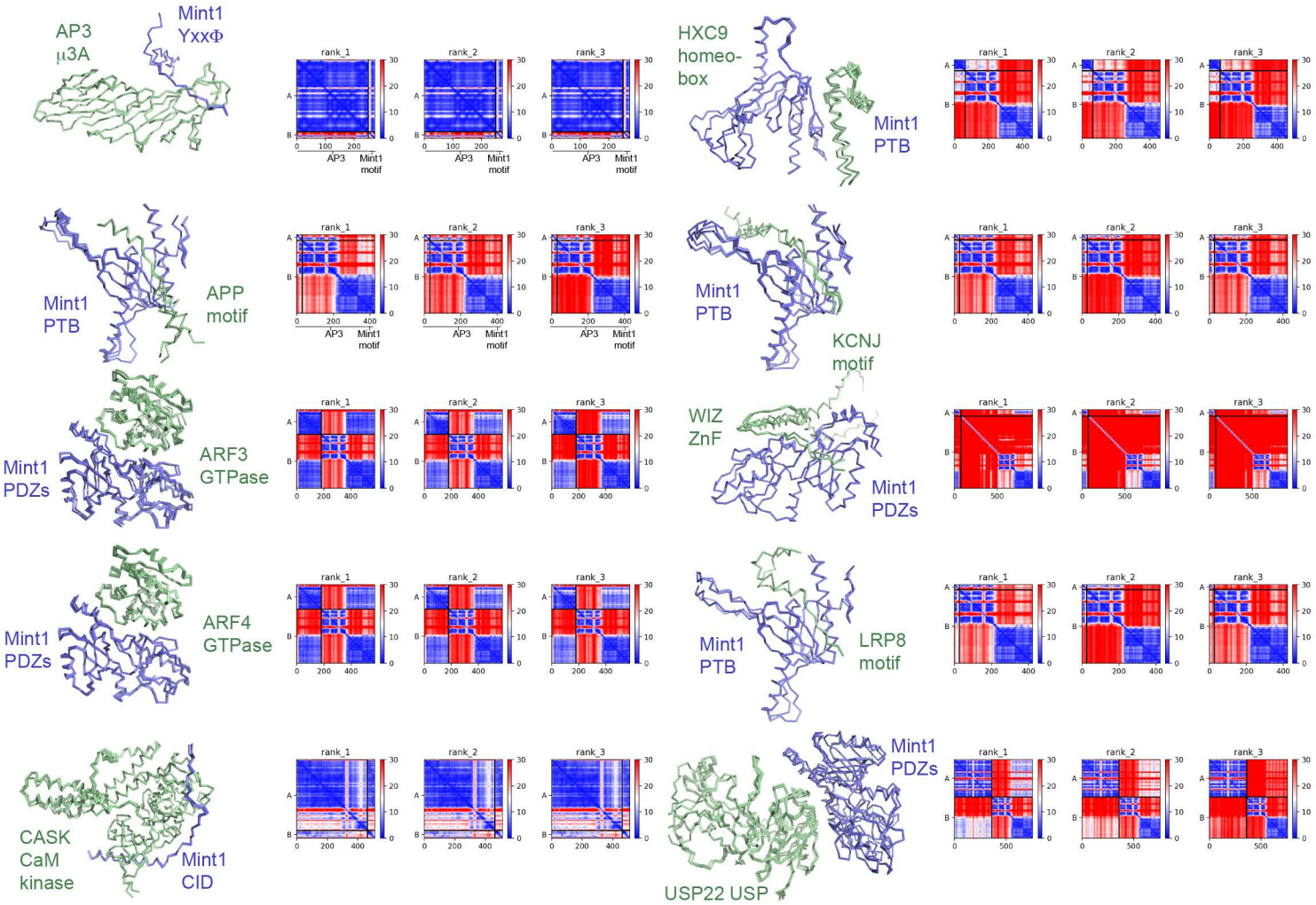

Figure S6. AlphaFold2 modelling of Mint1 interactions with proteins identified in BioGRID. (Related to Fig. 5 and 6)
Proteins identified in BioGRID as putative interactors of Mint1 and showing reasonable binding in AlphaFold2 predictions. The left panels show the top three ranked structures overlaid in backbone ribbon representation. On the right hand side the predicted alignment error (PAE) is plotted for each model. Signals in the off-diagonal regions indicate strong structural correlations between residues in the peptide with the Mint1 protein. These focused predictions were performed on specific Mint1 domains with the ligand regions initially identified in high-throughput predictions of the two full-length proteins.

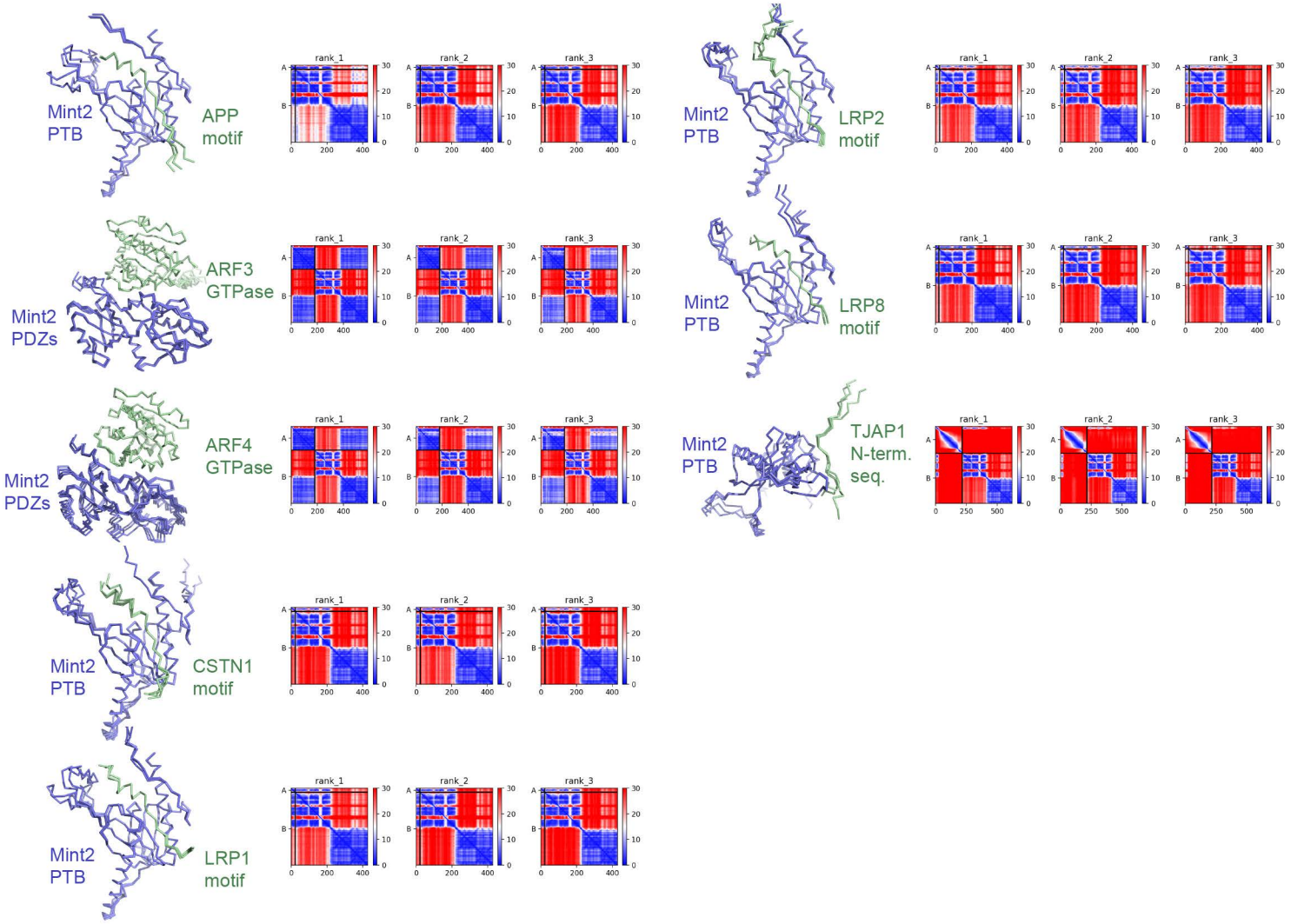

Figure S7. AlphaFold2 modelling of Mint2 interactions with proteins identified in BioGRID. (Related to Fig. 5 and 6)
Proteins identified in BioGRID as putative interactors of Mint2 and showing reasonable binding in AlphaFold2 predictions. The left panels show the top three ranked structures overlaid in backbone ribbon representation. On the right hand side the predicted alignment error (PAE) is plotted for each model. Signals in the off-diagonal regions indicate strong structural correlations between residues in the peptide with the Mint2 protein. These focused predictions were performed on specific Mint2 domains with the ligand regions initially identified in high-throughput predictions of the two full-length proteins.